Spectrochimica Acta Part A: Molecular and Biomolecular Spectroscopy 358 (2026) 127898

Contents lists available at ScienceDirect

Spectrochimica Acta Part A:
Molecular and Biomolecular Spectroscopy

journal homepage: www.journals.elsevier.com/spectrochimica-acta-part-a-molecular-and-biomolecular-spectroscopy

Thermally robust dual-band anti-thermal quenching in alkali-co-doped $K_7SrGd_2(B_5O_{10})_3$:Tb^{3+} phosphors

Abeer S. Altowyan [a,**], R. Tulek [b], A. Teke [b], M.B. Coban [b], C. Gok [c], U.H. Kaynar [c,d], Jabir Hakami [e], H. Aydin [f,g], N. Can [e,*]

[a] Department of Physics, College of Science, Princess Nourah Bint Abdulrahman University, P.O. Box 84428, Riyadh 11671, Saudi Arabia
[b] Balikesir University, Faculty of Arts and Sciences, Department of Physics, Balikesir, Turkiye
[c] Bakırçay University, Biomedical Technologies Design Application and Research Center, Menemen, Izmir, Turkiye
[d] Bakırcay University, Faculty of Engineering and Architecture, Department of Fundamental Sciences, Menemen, Izmir, Turkiye
[e] Jazan University, College of Science, Department of Physical Sciences, Physics Division, P.O. Box 114, 45142 Jazan, Saudi Arabia
[f] Central Research Laboratories, Izmir Katip Celebi University, Izmir, Turkiye
[g] Graphene Application &Research Center, Izmir Katip Celebi University, Izmir, Turkiye

HIGHLIGHTS

- Dual-band anti-thermal quenching is achieved in $K_7SrGd_2(B_5O_{10})_3$:Tb^{3+} phosphors.
- Both green and red Tb^{3+} emissions intensify with increasing temperature up to 550 K.
- Alkali co-doping enhances luminescence while maintaining millisecond-scale lifetimes.
- Anti-thermal behavior originates from thermally activated energy feeding mechanisms.
- The phosphors are promising for high-temperature photonic applications.

GRAPHICAL ABSTRACT

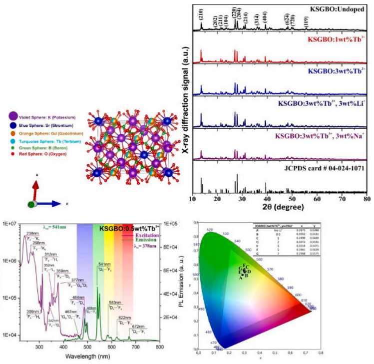

ARTICLE INFO

Keywords:
$K_7SrGd_2(B_5O_{10})_3$
Tb doping
Photoluminescence
Anti-thermal quenching
Dual-band emission
Thermal stability

ABSTRACT

In this study, Tb^{3+}-activated $K_7SrGd_2(B_5O_{10})_3$ (KSGBO) phosphors, with and without alkali ion (Li^+/Na^+) co-doping, were synthesized via a combustion method and systematically investigated for their structural and photoluminescence properties. Rietveld-refined XRD analysis confirmed the formation of a trigonal pentaborate phase (space group R32), with Tb^{3+} ions substituting at Gd^{3+} sites. Alkali co-doping induced a slight unit cell contraction (~0.22%for Li^+ and ~ 0.26% for Na^+), indicating lattice relaxation. Under 378 nm excitation, the phosphors exhibited intense dual-band Tb^{3+} emission—green ($^5D_4 \rightarrow {}^7F_5$, 541 nm) and red ($^5D_4 \rightarrow {}^7F_4$, 672 nm)—with maximum intensity at 3 wt% Tb^{3+}, beyond which concentration quenching occurs. Remarkably, both emission bands showed anti-thermal quenching behavior, with the 541 nm emission intensity increasing by nearly twofold between 300 and 550 K, demonstrating exceptional thermal stability. For Li^+ and Na^+ co-doped samples, thermally activated enhancement followed by quenching was supported by activation energy values of

---

* Corresponding author.
** Corresponding author.
E-mail addresses: asaltowyan@pnu.edu.sa (A.S. Altowyan), ncan@jazanu.edu.sa (N. Can).

https://doi.org/10.1016/j.saa.2026.127898
Received 12 January 2026; Received in revised form 30 March 2026; Accepted 10 April 2026
Available online 12 April 2026

0.349 eV (Li^+) and 0.304 eV (Na^+). Additionally, alkali co-doping significantly enhanced the emission intensity, with ~4.5-fold (Li^+) and ~ 3-fold (Na^+) increases compared to the undoped sample. Time-resolved PL measurements revealed millisecond-scale decay lifetimes, with the average lifetime slightly decreasing from 1.25 ms (Tb^{3+} only) to 1.15 ms (Li^+) and 1.20 ms (Na^+), while maintaining efficient radiative recombination. Furthermore, CIE analysis demonstrated improved color purity, reaching up to 92% in Li^+ co-doped samples, along with tunable chromaticity. These combined effects—dual-band emission, quantified anti-thermal enhancement, and co-doping-induced intensity amplification—highlight KSGBO:Tb^{3+} phosphors as promising candidates for high-temperature optoelectronic and solid-state lighting applications.

1. Introduction

Complex borate compounds containing alkali, alkaline-earth, and rare-earth cations have attracted considerable attention due to their rich crystal chemistry, high thermal stability, and favorable optical characteristics [1–3]. The coexistence of trigonal (BO_3) and tetrahedral (BO_4) units in borate systems enables the formation of structurally rigid and thermally stable polyborate frameworks [4]. Among these systems, borates constructed from pentaborate [B_5O_{10}] units are particularly interesting, as the coexistence of BO_3 and BO_4 polyhedra enables the formation of rigid and thermally stable networks. Such pentaborate-based frameworks represent an important structural motif in rare-earth borates, providing mechanically robust lattices suitable for both structural and optical investigations [5].

In such structures, rare-earth ions commonly play a dual role by acting as structural linkers through RE–O polyhedra and as optically active centers, while alkali and alkaline-earth cations provide charge compensation and stabilize the lattice. Similar structural features have been reported in Gd-based pentaborate systems, where isolated [B_5O_{10}] clusters are interconnected via REO_6 octahedra and charge-balanced by alkali or alkaline-earth cations [5,6].

Among them, $K_7SrGd_2(B_5O_{10})_3$ (KSGBO) represents a promising mixed-cation rare-earth borate host lattice in which Gd^{3+} ions are an integral part of the crystal framework rather than extrinsic dopants. The coexistence of K^+, Sr^{2+}, and Gd^{3+} cations is expected to influence local symmetry, coordination environments, and lattice distortion, which are critical factors governing the optical behavior of rare-earth ions.

The presence of polyborate $(B_5O_{10})^{5-}$ clusters, combined with mixed cation environments, makes this compound particularly attractive for photoluminescent and high-temperature optical applications. In rigid borate lattices, the local coordination symmetry and bonding environment of rare-earth ions are key factors governing radiative transition probabilities and emission characteristics. Consequently, rare-earth borates such as $YAl_3(BO_3)_4$, $GdAl_3(BO_3)_4$, and $RECa_4O(BO_3)_3$ (RE = Y, Gd) have been extensively investigated as representative optical host materials [7–10].

Rare-earth (RE^{3+}) ions have attracted considerable attention due to their unique electronic configurations, which give rise to sharp emission bands spanning the visible and near-infrared regions. These characteristics make them highly suitable for a wide range of applications, including solid-state lighting, display technologies, optical amplifiers, lasers, and sensing devices. In particular, RE ions such as Eu^{3+}, Sm^{3+}, Er^{3+}, Dy^{3+}, and Tb^{3+} have been extensively studied for their tunable luminescence properties and high color purity in photonic materials.

Among them, Sm^{3+} ions are well known for their efficient orange-red emission and applications in display and laser systems [11]. Tb^{3+} ions are particularly attractive among rare-earth activators due to their intense green emission originating from the $^5D_4 \rightarrow {}^7F_5$ transition, making them highly suitable for green-emitting phosphors in solid-state lighting and display applications. In addition, Tb^{3+} ions exhibit relatively high quantum efficiency and thermal stability compared to other RE ions. In particular, the choice of host lattice plays a crucial role in determining the luminescence efficiency and thermal stability of rare-earth-doped phosphors. Rare-earth ions embedded in rigid borate lattices are well known to exhibit sharp f–f electronic transitions, low phonon-assisted nonradiative losses, and good thermal stability of luminescence. In particular, Tb^{3+}-activated borate phosphors have been extensively investigated due to their intense green emission originating from the $^5D_4 \rightarrow {}^7F_5$ transition and their high color purity [12–17]. Various Tb^{3+}-doped borate hosts have demonstrated that the rigid borate framework effectively suppresses nonradiative relaxation processes, resulting in enhanced emission intensity and thermal stability [18–20]. When combined with CIE chromaticity analysis, photoluminescence studies enable a comprehensive assessment of the emission characteristics and color tunability of rare-earth-based phosphor materials.

In addition to these studies, several Tb^{3+}-activated borate phosphors such as $YAl_3(BO_3)_4$:Tb^{3+} [8,21], $YBa_3(BO_3)_3$:Tb^{3+} [18], $GdAl_3(BO_3)_4$:Ln^{3+} (Ln^{3+}:Eu^{3+}, Tb^{3+}, Dy^{3+}) [3,22], $Sr_3Gd(BO_3)_3$:Tb^{3+} [23], $K_3Y(BO_2)_6$:Tb^{3+} [24], and $Na_2Gd_2B_2O_7$:Tb^{3+} [25], $K_7CaY_2(B_5O_{10})_3$:Tb^{3+} [15] have been extensively reported, exhibiting strong green emission arising from the $^5D_4 \rightarrow {}^7F_5$ transition with high color purity and good thermal stability. Compared with these reported borate hosts, the present $K_7SrGd_2(B_5O_{10})_3$:Tb^{3+} system exhibits comparable or enhanced photoluminescence performance, particularly in terms of pronounced anti-thermal quenching behavior and significant emission intensity enhancement induced by alkali co-doping, highlighting its potential for high-temperature photonic applications.

Among various borate-based hosts, $K_7SrGd_2(B_5O_{10})_3$ offers a unique structural platform in which Gd^{3+} ions are intrinsic lattice constituents, providing a chemically compatible and energetically favorable site for Tb^{3+} substitution. In addition, the rigid pentaborate framework and the presence of alkali-rich cationic environments make this host particularly suitable for achieving thermally robust luminescence and for systematically tuning optical properties via alkali co-doping.

Therefore, the present work aims to address the limited understanding of Tb^{3+}-activated $K_7SrGd_2(B_5O_{10})_3$ phosphors and to systematically investigate the role of alkali co-doping in tailoring their structural and photoluminescence properties. The motivation of this study stems from the unique structural characteristics of the KSGBO host lattice, in which Gd^{3+} acts as an intrinsic lattice constituent, providing a chemically compatible and energetically favorable substitution site for Tb^{3+} ions within a rigid pentaborate framework. Moreover, the alkali-rich environment of this host offers a versatile platform for tuning local symmetry, defect states, and energy transfer processes through controlled Li^+/Na^+ incorporation.

The originality of this work lies in the first comprehensive investigation of Tb^{3+}-activated KSGBO phosphors with alkali co-doping, revealing several distinctive and previously unexplored features. In particular, the system exhibits thermally robust dual-band emission with anti-thermal quenching behavior, where both green and red emissions are simultaneously enhanced with increasing temperature. Furthermore, alkali co-doping leads to significant photoluminescence enhancement and improved color characteristics, while maintaining favorable recombination dynamics. The enhanced thermal stability, supported by activation energy analysis, further highlights the resistance of these materials to thermally activated non-radiative processes.

These combined features underline the potential of KSGBO:Tb^{3+} phosphors as promising candidates for next-generation temperature-stable green-emitting materials in solid-state lighting, display technologies, and optical thermometry.

2. Experimental procedure

2.1. Materials and synthesis

High-purity K_2CO_3, $SrCO_3$, H_3BO_3, and Gd_2O_3 (≥99.9%, Sigma-Aldrich) were selected as precursor materials for the preparation of the $K_7SrGd_2(B_5O_{10})_3$ host lattice. Tb_4O_7 (≥99.99%, Alfa Aesar) was employed as the activator ion and incorporated into the lattice by substituting Gd^{3+} sites at concentrations ranging from 0.5 to 7 wt%. To examine the influence of alkali co-doping on the material properties, analytical-grade Li_2CO_3 and Na_2CO_3 were introduced in amounts between 0.5 and 7.0 wt%. All starting compounds were weighed according to their stoichiometric ratios and thoroughly homogenized in an agate mortar. A small amount of deionized water was added to assist mixing and to obtain a uniform slurry. The resulting mixture was dried at 120 °C to remove residual moisture and then subjected to a conventional solid-state synthesis procedure. The dried powders were initially calcined at 600 °C for 4 h to eliminate volatile species and facilitate precursor decomposition. After regrinding, the powders were annealed at 950 °C for 6 h in ambient air to promote phase development and crystallization. Following natural cooling to room temperature, the final products were stored in airtight containers to prevent moisture absorption. This synthesis approach enabled the successful incorporation of Tb^{3+} ions into the Gd^{3+} sites of the pentaborate host structure, resulting in single-phase $K_7SrGd_2(B_5O_{10})_3$ phosphors with good crystallinity and compositional uniformity, suitable for subsequent structural and spectroscopic investigations. Notation "x" used in sample compositions (e.g., KSGBO: $x$$Tb^{3+}$) corresponds to x wt% of Tb^{3+}. This convention is adopted consistently throughout the manuscript.

2.2. Structural characterization

The synthesized KSGBO phosphors were systematically investigated to elucidate their structural, vibrational, morphological, and optical characteristics using a combination of complementary experimental techniques. Phase purity and crystallographic properties were analyzed by powder X-ray diffraction (XRD) employing a Malvern Panalytical Empyrean diffractometer with Cu Kα radiation ($\lambda = 1.5406$ Å). Diffraction patterns were recorded in the 2θ range of 10–80° with a step size of 0.02°. Structural parameters, average crystallite size, and phase composition were determined through Rietveld refinement using the HighScore Plus software package. Fourier transform infrared (FTIR) spectroscopy was performed using a Thermo Scientific Nicolet iS50 spectrometer over the wavenumber range of 400–4000 cm^{-1} to identify characteristic vibrational modes and bonding environments within the borate framework. Raman spectra were acquired with a Renishaw in Via Raman microscope equipped with a 532 nm excitation laser and a 2400 lines mm^{-1} grating. Measurements were carried out in the spectral region of 100–3200 cm^{-1} to examine vibrational features associated with BO_3 and BO_4 structural units, as well as possible dopant-induced lattice distortions. The surface morphology and elemental composition of the samples were examined by scanning electron microscopy (SEM) coupled with energy-dispersive X-ray spectroscopy (EDS) using a ZEISS GeminiSEM 500 operated at an accelerating voltage of 20 kV under high-vacuum conditions. Prior to analysis, a thin gold coating was applied to the sample surfaces to minimize charging effects. SEM micrographs were utilized to assess particle morphology, grain connectivity, and agglomeration behavior, while EDS analysis provided qualitative and quantitative information on elemental distribution and dopant incorporation. Photoluminescence (PL) excitation and emission spectra were recorded using an Edinburgh Instruments FS5 spectrofluorometer equipped with a 150 W xenon lamp. The luminescence behavior of Tb^{3+} ions was evaluated based on characteristic excitation and emission transitions. Time-resolved PL decay measurements were carried out using the same system to determine luminescence lifetimes. Colorimetric properties were assessed by calculating the Commission Internationale de l'Éclairage (CIE) chromaticity coordinates from the emission spectra.

3. Results and discussions

3.1. Crystal structure analysis, Rietveld refinement, and site occupancy evaluation

The crystallographic characteristics, phase composition, and structural stability of both undoped and Tb^{3+}-doped KSGBO phosphors, including compositions co-doped with Li^+ and Na^+ ions, were comprehensively examined by means of powder X-ray diffraction (XRD) coupled with Rietveld refinement techniques. The diffraction profiles illustrated in Fig. 1a demonstrate that all observed Bragg reflections correspond well with those listed in the standard JCPDS database (Card No. 04–024-1071), thereby verifying the successful formation of a pure KSGBO phase. Further analysis of the diffraction data reveals that the KSGBO host adopts a trigonal lattice belonging to the R32 space group. Within the detection limits of the measurement system, no extraneous diffraction peaks attributable to secondary phases or impurity-related compounds are observed. These results clearly indicate that neither rare-earth ion incorporation nor alkali metal co-doping induces any detectable disruption to the fundamental crystal framework of the host material.

The overall similarity in peak positions and relative intensities among all compositions suggests that the long-range crystal symmetry remains unchanged upon Tb^{3+} incorporation and subsequent Li^+/Na^+ co-doping. Minor variations in peak intensity are attributed to subtle differences in crystallinity and microstructural effects rather than phase transformation. These results demonstrate that the KSGBO framework exhibits sufficient structural tolerance to accommodate dopant and co-dopant ions without inducing detectable lattice instability.

A schematic representation of the KSGBO crystal structure is illustrated in Fig. 1b, highlighting the three-dimensional borate network constructed from interconnected boron–oxygen polyhedral units. The Gd^{3+} ions are octahedrally coordinated by oxygen atoms and serve as structural linkers between isolated $[B_5O_{10}]$ clusters. Within this rigid framework, K^+, Sr^{2+}, and Gd^{3+} ions occupy distinct crystallographic sites coordinated by oxygen atoms. The Gd^{3+} sites, in particular, provide a chemically compatible environment for Tb^{3+} substitution due to their identical valence state and comparable coordination geometry, while the overall framework maintains charge neutrality and structural coherence. Since Tb^{3+} and Gd^{3+} possess the same trivalent oxidation state, this substitution occurs without the need for additional charge compensation mechanisms.

Rietveld refinement was carried out to quantitatively evaluate the structural parameters of all samples. Representative refinement profiles are shown in Fig. 1c, where a close correspondence between the observed and calculated diffraction patterns is observed. The difference curves remain nearly flat across the full 2θ range, indicating the absence of systematic misfits. The obtained reliability factors fall within acceptable limits, with χ^2 values ranging from 2.07 to 2.63, R_p values between 0.041 and 0.049, and R_{wp} values in the range of 0.057–0.068, confirming the consistency of the applied structural model. Although crystallite size and microstrain parameters are typically not the primary focus of Rietveld refinement, preliminary estimates of crystallite broadening can be obtained from profile fitting. These values, along with more detailed microstructural analyses, are further evaluated in Section 3.2 using multiple line broadening models for comparative accuracy and robustness. The refined lattice parameters and agreement indices are summarized in Table 1. Only marginal variations in lattice constants and unit cell volume are observed upon Tb^{3+} doping, while a slight unit-cell contraction is observed for Li^+ and Na^+ co-doped samples, which can be attributed to lattice relaxation effects associated with local charge compensation. The selection of Li^+ and Na^+ as co-dopants is driven by their relatively smaller ionic radii (0.76 Å for Li^+ and 1.02 Å

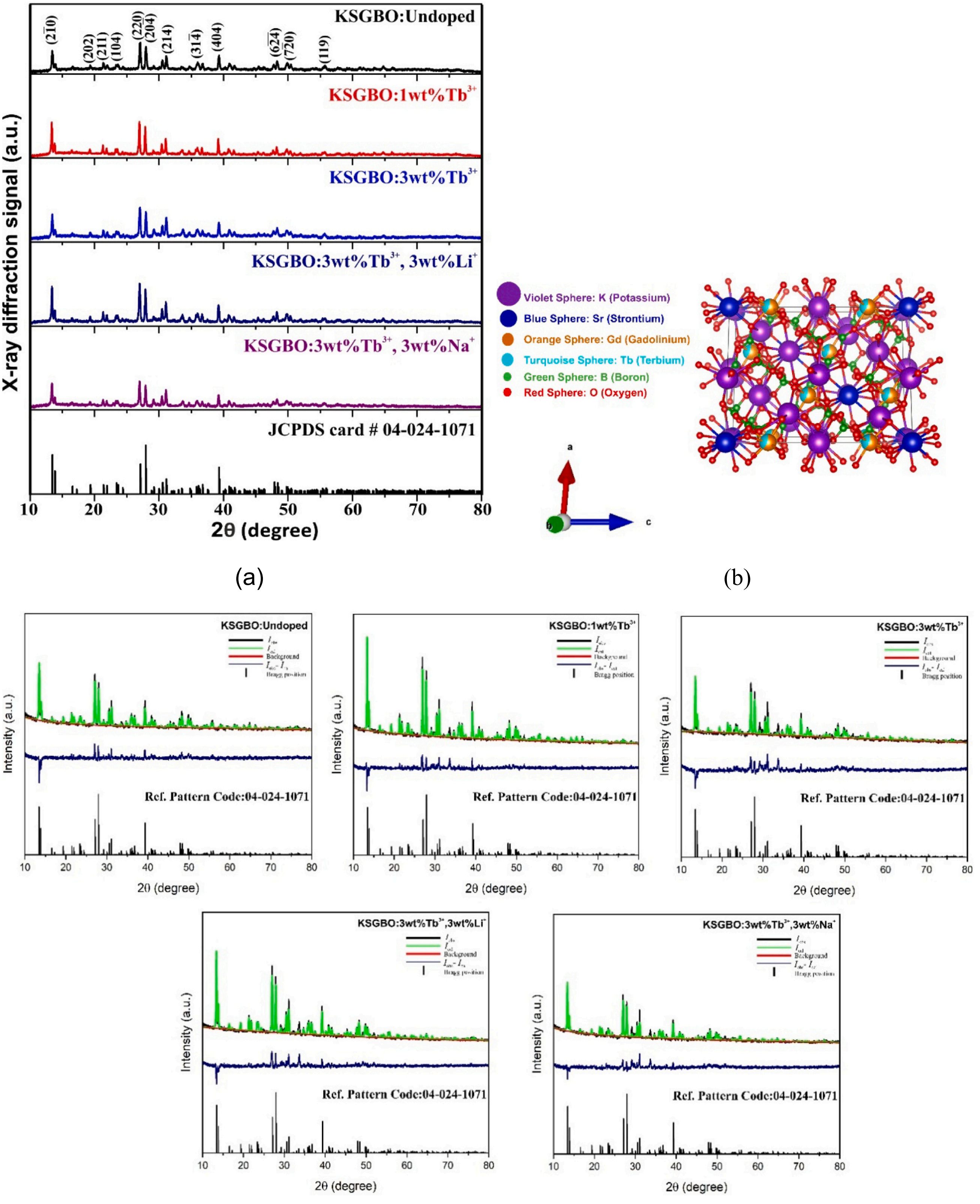

(a)

(b)

(c)

Fig. 1. (a) X-ray diffraction patterns of undoped and Tb^{3+}-doped KSGBO phosphors, including Li^{+} and Na^{+} co-doped compositions, indexed to the standard JCPDS card No. 04–024-1071.
(b) Schematic crystal structure of KSGBO illustrating the three-dimensional borate framework and cationic site distribution. (c) Representative Rietveld refinement profiles of KSGBO samples showing observed, calculated, and difference patterns.

Table 1

Refined lattice parameters and Rietveld reliability factors of undoped and Tb^{3+}-doped KSGBO phosphors, including Li^+ and Na^+ co-doped compositions.

	KSGBO				
Unit Cell	Undoped	1wt%Tb^{3+}	3wt%Tb^{3+}	3wt%Tb^{3+}, 3wt%Li^+	3wt%Tb^{3+}, 3wt%Na^+
a [Å]	13.21	13.19	13.20	13.19	13.20
b [Å]	13.21	13.19	13.20	13.19	13.20
c [Å]	15.41	15.41	15.38	15.41	15.39
α, β, γ [°]	90,90,120	90,90,120	90,90,120	90,90,120	90,90,120
Vol. [Å^3]	2330.82	2324.37	2324.782	2325.663	2324.833
χ^2	2.13	2.071	2.626	2.229	2.065
R_p	0.04	0.041	0.049	0.044	0.044
R_{wp}	0.061	0.057	0.067	0.060	0.059
R_{exp}	0.028	0.027	0.025	0.027	0.028

for Na^+) compared to K^+ (1.38 Å), enabling partial substitution or interstitial incorporation within K^+-rich sites of the KSGBO lattice. This controlled size mismatch is expected to introduce localized lattice strain and electrostatic potential fluctuations, which may modulate point defect populations and suppress non-radiative recombination pathways. Similar alkali co-doping strategies have been reported to improve crystallinity, lattice stability, and photoluminescence efficiency in rare-earth-doped borate systems [19]. Such contraction likely arises from the incorporation of smaller monovalent ions (Li^+/Na^+) into the K^+-rich sites of the trigonal lattice, potentially inducing local strain and subtle modifications in the polyhedral environment. These local distortions, although not visible in long-range XRD patterns, may influence defect states or site symmetry — factors which are further investigated in the optical and microstructural analyses in subsequent sections. Based on the refined unit-cell volumes, the contraction amounts to approximately 0.22% for the Li^+-co-doped sample and 0.26% for the Na^+-co-doped sample relative to the undoped composition.

To further clarify the preferred substitution site of Tb^{3+} ions, the ionic radius mismatch (D_r) was evaluated using Shannon's effective ionic radii for sixfold coordination. The calculated D_r values, summarized in Table 2, indicate a minimal mismatch of 1.599% between Tb^{3+} (0.923 Å) and Gd^{3+} (0.938 Å), whereas larger mismatches are obtained for potential substitution at Sr^{2+} (6.135%) and K^+ (31.115%) sites. Considering that a radius mismatch below 30% is generally required for stable substitutional doping, these results indicate that Tb^{3+} ions preferentially occupy Gd^{3+} lattice sites.

In the KSGBO host lattice, Tb^{3+} substitution at Gd^{3+} sites does not require charge compensation due to identical trivalent oxidation states. However, the subsequent introduction of Li^+ and Na^+ ions represents an additional modification to the alkali-rich framework rather than a charge-balancing necessity. Given the presence of multiple crystallographically distinct K^+ sites, alkali co-doping is expected to induce local lattice relaxation and charge redistribution without disrupting the long-range crystal symmetry, as confirmed by the absence of secondary phases in Fig. 1a. The slight unit-cell contraction observed in Table 1 further supports the occurrence of localized structural adjustments, which are commonly associated with alkali-assisted modulation of defect environments and luminescence efficiency in complex borate lattices.

Overall, the combined XRD, Rietveld refinement, and ionic radius mismatch analyses consistently demonstrate that Tb^{3+} incorporation and alkali co-doping do not compromise the structural stability of the KSGBO host lattice. This structurally coherent framework provides a reliable basis for interpreting the photoluminescence behaviours discussed in the following sections. These findings confirm that the observed structural stability is intrinsic to the host lattice rather than being influenced by secondary phase formation.

3.2. *Crystallite size and microstrain evaluation via line broadening methods*

To further understand the microstructural features of KSGBO phosphors beyond the average structural analysis provided by Rietveld refinement, several line broadening approaches were employed to estimate crystallite size and microstrain. To obtain more accurate estimates of crystallite size and microstrain beyond the Rietveld-derived average structure, several line broadening models were employed, including the Debye–Scherrer, Monshi–Scherrer[26], Williamson–Hall [27], Halder–Wagner [28], and Size–Strain Plot methods [29]. These complementary approaches enable the distinction between size-induced and strain-induced broadening effects and reveal the influence of rare-earth and alkali co-doping on the nanocrystalline structure of the phosphors.

All applied methods consistently show that Tb^{3+} doping leads to a marked increase in average crystallite size, regardless of the model used. This growth in crystallite size is associated with enhanced crystallinity and reduced structural imperfections, due to the substitution of Tb^{3+} at Gd^{3+} sites with minimal ionic mismatch. As observed in the Monshi–Scherrer and Williamson–Hall plots (Fig. 2a and b), the slopes of the linear fits decrease progressively with increasing Tb^{3+} content, reflecting narrower diffraction peaks and reduced internal strain.

The H—W model (Fig. 2c), known for its sensitivity to well-crystallized systems, provides additional confirmation of this trend by showing steeper slopes in the undoped sample, indicating higher strain. The SSP method (Fig. 2d), which accounts for both crystallite size and strain in a unified plot, supports these findings and provides the most balanced estimation of microstructural parameters.

Alkali ion co-doping with Li^+ and Na^+ results in a minor reduction in crystallite size and a minor increase in microstrain compared to the Tb^{3+}-only doped samples. This effect is attributed to local lattice distortions caused by the incorporation of smaller monovalent ions, which create localized stress fields but do not significantly compromise the long-range structural order. Still, the co-doped compositions maintain superior microstructural properties compared to the undoped sample.

Overall, the combined line broadening analyses (Figs. 2a–2d) indicate that Tb^{3+} doping improves crystallite coherence and minimizes microstrain, while alkali co-doping introduces manageable local distortions. These microstructural refinements are expected to reduce non-

Table 2

Calculated ionic radius mismatch (D_r) values for possible substitution sites of Tb^{3+} ions in the KSGBO lattice based on Shannon's effective ionic radii.

	K		Tb			Sr		Tb			Gd		Tb	
D_r	R_m	CN	R_d	CN	**D_r**	R_m	CN	R_d	CN	**D_r**	R_m	CN	R_d	CN
31.11	1.38	6	0.92	6	6.13	1.1	6	0.92	6	1.59	0.93	6	0.92	6

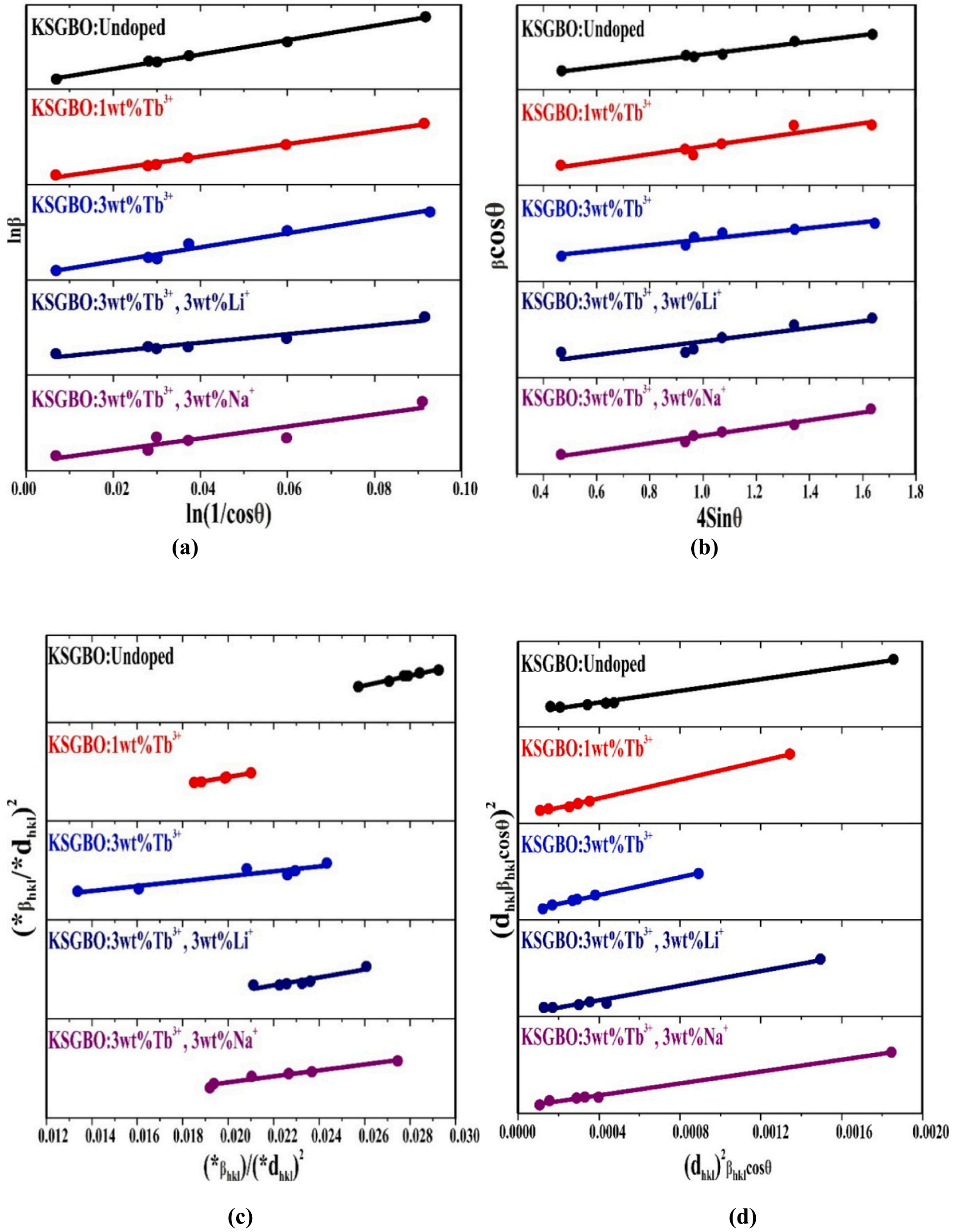

Fig. 2. (a) Monshi–Scherrer plot (lnβ vs ln(1/cosθ)) for undoped and doped KSGBO samples, showing reduced slopes with increasing dopant concentration, indicating higher crystallinity. (b). Williamson–Hall plot (βcosθ vs 4sinθ) illustrating strain reduction trends in Tb^{3+}-doped and co-doped samples. (c) Halder–Wagner plot, emphasizing the contrast in slope steepness between undoped and doped KSGBO, confirming reduced lattice strain. (d) Size–Strain Plot (SSP) analysis combining both size and strain effects for comprehensive evaluation of microstructural changes.

radiative centers and positively influence the photoluminescence behavior of the phosphor system.

The numerical values of crystallite size and microstrain obtained from the above-mentioned models are summarized in Table 3.

3.3. *Vibrational analysis via FTIR and Raman spectroscopy*

To explore the short-range ordering and local bonding environment within KSGBO phosphors, Fourier-transform infrared (FTIR) and Raman spectroscopic techniques were utilized. These methods are effective for probing the vibrational characteristics of borate groups and identifying structural modifications resulting from Tb^{3+} doping and alkali metal co-doping.

The FTIR spectra for both undoped and Tb^{3+}-doped KSGBO samples are depicted in Fig. 3a. A broad absorption peak located at approximately 3429 cm^{-1} is attributed to the O—H stretching vibrations, which likely originate from surface-bound water molecules or hydroxyl groups. Additional absorption bands observed in the 1600–400 cm^{-1} range correspond to intrinsic vibrational modes associated with the borate framework.

Table 3

Crystallite size (D) and microstrain (ε or δ) values for undoped and $Tb^{3+}/Li^{+}/Na^{+}$ doped KSGBO phosphors calculated using different line broadening models.

Concentration		Undoped	1wt% Tb^{3+}	3wt% Tb^{3+}	3wt% Tb^{3+}, 3wt% Li^{+}	3wt% Tb^{3+}, 3wt% Na^{+}
Debye-Scherer	D (nm)	68.03	95.77	98.40	81.58	85.89
	$\delta \times 10^{-3}$ (nm^{-2})	0.21	0.10	0.10	0.15	0.13
Monshi-Scherrer	D (nm)	65.49	94.90	96.42	78.09	84.47
	$\delta \times 10^{-3}$ (nm^{-2})	0.23	0.1110	0.10	0.16	0.14
Williamson-Hall	D (nm)	72.77	95.90	101.27	79.56	82.75
	$\varepsilon \times 10^{-3}$	2.46	2.29	1.31	1.63	2.50
Halder-Wagner	D (nm)	68.49	96.15	108.69	81.96	86.20
	$\varepsilon \times 10^{-3}$	11.13	8.00	6.92	9.59	9.95
Size-Strain	D (nm)	65.52	93.42	111.39	80.00	86.20
	$\varepsilon \times 10^{-3}$	2.19	1.78	1.09	1.54	1.41

Specifically, the bands at 1475 and 1428 cm^{-1} are attributed to the stretching vibrations of B—O bonds in trigonal $[BO_3]^{3-}$ units. The 1360–1110 cm^{-1} region reflects asymmetric B—O stretching, indicating the degree of cross-linking between borate polyhedra. The redshift observed in the B—O asymmetric stretching region with Tb^{3+}/Na^{+} co-doping suggests a rearrangement in borate coordination, in agreement with similar modifications reported in ytterbium-doped borate systems [30]. Additionally, the peaks at 729, 615, and 569 cm^{-1} are due to out-of-plane bending vibrations of B–O–B linkages, which are often sensitive to distortions in the glass network. The low-frequency band at 496 cm^{-1} is ascribed to the in-plane bending of $[BO_3]$ units [31].

Tb^{3+} doping and subsequent Li^{+}/Na^{+} co-doping induce modest band shifts and broadening, especially between 1000 and 600 cm^{-1}. These variations likely stem from local lattice stress and minor distortions caused by ionic substitution or interstitial incorporation. The presence of alkali ions, which possess different ionic radii compared to K^{+}, can induce non-uniform lattice deformation, resulting in asymmetrical vibrational behavior.

Fig. 3b displays the Raman spectra of all samples in the 100–3000 cm^{-1} range. The undoped KSGBO shows a well-defined set of Raman-active modes, consistent with the trigonal crystal structure and the presence of both $[BO_3]$ and $[BO_4]$ structural units. The peaks in the 500–1000 cm^{-1} region are primarily assigned to symmetric and asymmetric B—O stretching vibrations of $[BO_4]^{-}$and $[BO_3]^{3-}$ units. For instance, bands near 626 and 735 cm^{-1} correspond to symmetric stretching of $[BO_4]$, while those at 982 and 935 cm^{-1} are attributed to vibrations involving bridging oxygen atoms in mixed coordination environments [32].

At lower frequencies (<500 cm^{-1}), bands such as 161, 239, 290, and 394 cm^{-1} are associated with lattice phonons and metal–oxygen (Gd—O, Tb—O) interactions. These modes are sensitive to crystal field changes and can reflect cation substitution or local disorder. Notably, co-doped samples exhibit enhanced vibrational mode dispersion and reduced intensity, particularly in the 544–735 cm^{-1} range, suggesting increased phonon scattering and reduced long-range order. These spectral modifications support the idea of internal structural stress and distortion arising from ionic substitution and charge compensation mechanisms, consistent with previous studies on alkali-doped borates [19,32].

The combined FTIR and Raman analyses confirm the coexistence of trigonal $[BO_3]$ and tetrahedral $[BO_4]$ units in the KSGBO lattice. While the overall vibrational framework is preserved upon doping, subtle frequency shifts, mode expansion, and intensity changes reveal localized structural distortions. These effects become more prominent with alkali co-doping, suggesting that the incorporation of Li^{+} and Na^{+} induces mild symmetry breaking and localized lattice deformation in the borate network. Such distortions may influence phonon–exciton interactions and contribute to the optical behaviours discussed in subsequent sections.

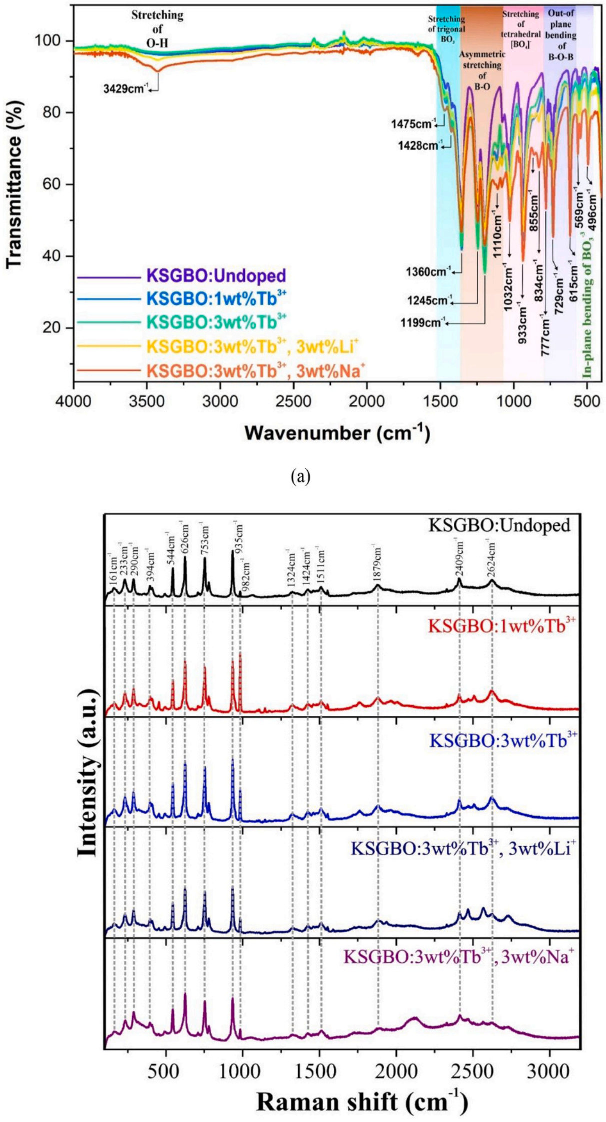

Fig. 3. (a) FTIR spectra of undoped and Tb^{3+}/alkali-doped KSGBO samples showing characteristic vibrations of BO_3 and BO_4 units. (b) Raman spectra of KSGBO phosphors with varying dopant content, highlighting structural changes in borate units and lattice vibrations.

3.4. Morphological and elemental analysis (SEM–EDS)

The microstructural characteristics and elemental composition of the synthesized KSGBO phosphors were examined by scanning electron microscopy (SEM) combined with energy-dispersive X-ray spectroscopy (EDS). Fig. 4a and Fig. 4b display the representative SEM images and corresponding EDS spectra of the undoped KSGBO and KSGBO:3wt% Tb^{3+} samples, respectively.

As observed in Fig. 4a, the undoped KSGBO sample consists of densely packed grains with irregular morphology and relatively smooth surfaces. The particles exhibit moderate agglomeration with well-

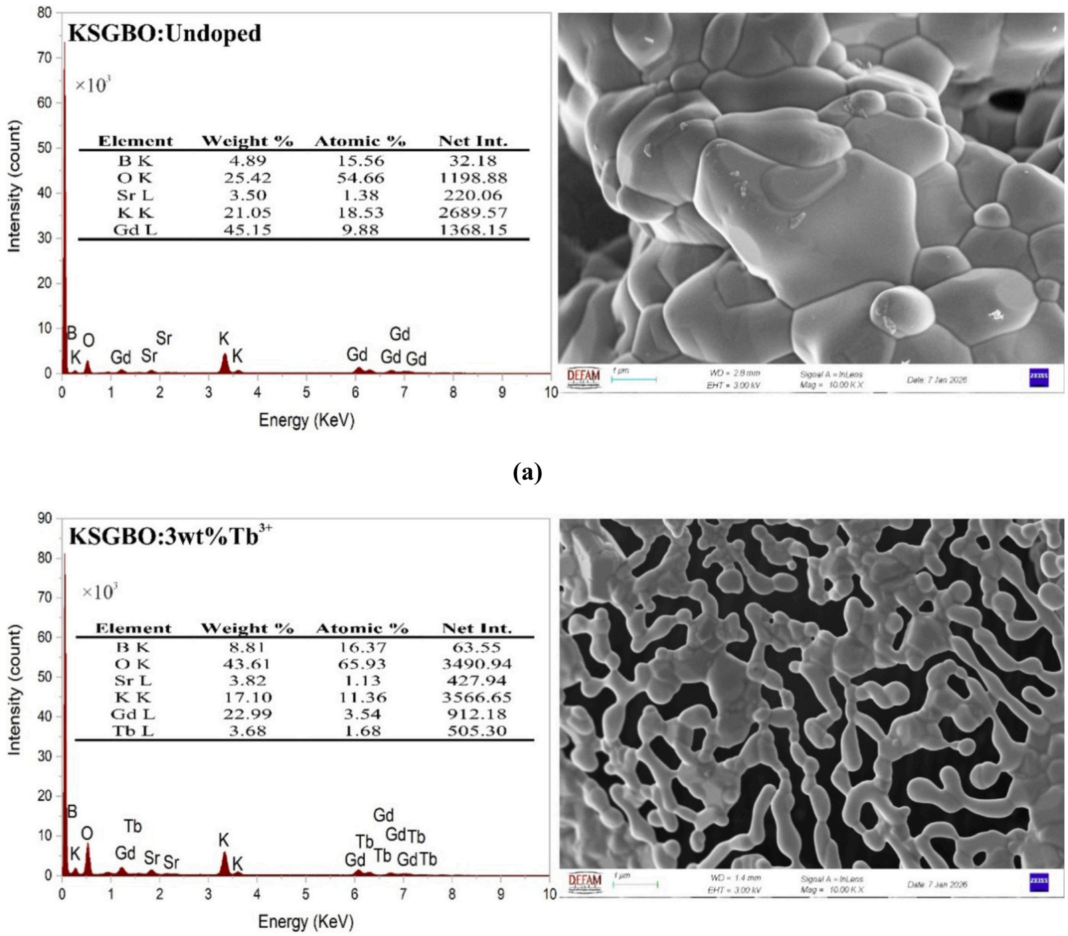

Element	Weight %	Atomic %	Net Int.
B K	4.89	15.56	32.18
O K	25.42	54.66	1198.88
Sr L	3.50	1.38	220.06
K K	21.05	18.53	2689.57
Gd L	45.15	9.88	1368.15

(a)

Element	Weight %	Atomic %	Net Int.
B K	8.81	16.37	63.55
O K	43.61	65.93	3490.94
Sr L	3.82	1.13	427.94
K K	17.10	11.36	3566.65
Gd L	22.99	3.54	912.18
Tb L	3.68	1.68	505.30

(b)

Fig. 4. SEM images and EDS spectra of (a) undoped KSGBO and (b) KSGBO: 3wt%Tb^{3+} phosphors, showing microstructural morphology and elemental composition. The presence of Tb signals in the doped sample confirms successful activator incorporation.

defined grain boundaries, which is typical for borate-based phosphors synthesized via high-temperature solid-state routes. The absence of abnormal grain growth or secondary morphologies suggests a uniform crystallization process and is consistent with the single-phase nature confirmed by XRD and Rietveld refinement. Such compact grain packing indicates good structural integrity of the KSGBO host lattice.

Upon Tb^{3+} incorporation, noticeable microstructural changes are observed, as shown in Fig. 4b. The KSGBO:3wt%Tb^{3+} phosphor exhibits a more porous and interconnected morphology, characterized by elongated grains and increased surface roughness. This morphological evolution can be attributed to dopant-induced modifications in lattice diffusion and grain growth kinetics during synthesis. The substitution of Tb^{3+} for Gd^{3+}—despite their similar ionic radii—can locally perturb the crystal lattice, promoting the formation of interconnected microstructures. Such porous morphologies are favorable for photoluminescent performance due to enhanced light scattering and extraction.

The chemical composition of both samples was further analyzed by EDS, and the corresponding spectra are included in Fig. 4a and b. For the undoped KSGBO sample, the EDS results confirm the presence of K, Sr, Gd, B, and O elements, in good agreement with the nominal stoichiometry of the host lattice. No impurity-related peaks are detected, indicating high phase purity.

For the Tb^{3+}-doped sample, additional Tb-related signals are observed in the EDS spectrum, confirming the successful incorporation of Tb^{3+} ions into the KSGBO lattice. It should be noted that the characteristic L-line X-ray emissions of Gd and Tb appear in closely spaced energy regions due to their adjacent atomic numbers. As a result, partial overlap of Gd and Tb peaks is observed in conventional SEM–EDS spectra, which is a well-known limitation of the technique when analyzing neighbouring lanthanide elements. Nevertheless, the systematic appearance of Tb signals in the doped sample, together with the compositional differences relative to the undoped KSGBO and the absence of any secondary phases, clearly verifies the presence of Tb^{3+} ions within the host matrix.

Importantly, no evidence of elemental segregation or Tb-rich secondary phases is detected, indicating a homogeneous distribution of the activator ions. When considered alongside the structural results obtained from XRD, ionic radius mismatch analysis, and the characteristic Tb^{3+} photoluminescence emissions, the SEM–EDS findings provide complementary confirmation that Tb^{3+} ions are successfully incorporated into Gd^{3+} lattice sites without disrupting the structural integrity of the KSGBO framework.

Overall, the combined SEM and EDS analyses demonstrate that Tb^{3+} doping induces controlled microstructural modifications while preserving chemical homogeneity and phase purity. These features are expected to play a beneficial role in the enhanced photoluminescence efficiency and thermal stability discussed in the subsequent sections.

3.5. *Photoluminescence properties of Tb^{3+}-activated KSGBO phosphors*

The photoluminescence (PL) properties of KSGBO phosphors activated with Tb^{3+} ions were systematically examined through excitation and emission spectroscopy to elucidate their optical behavior. The excitation spectrum of the sample with 0.5 wt% Tb^{3+} concentration (Fig. 5a), monitored at the green emission wavelength of 541 nm, reveals several sharp bands in the UV region. These bands correspond to the intra-$4f^8$ electronic transitions of Tb^{3+} ions from the ground state ($^7F_6$) to higher energy states such as $^5K_7$ (238 nm), $^5K_6$ (268 nm), $^5H_4$ (306 nm), $^5H_7$ (312 nm), $^5L_9$ (352 nm), $^5D_2$ (359 nm), $^5G_6/^5D_3$ (377 nm), and $^5D_4$ (484 nm). Although these f–f transitions are formally parity-forbidden, they gain intensity through 4f–5d configuration mixing and vibronic coupling mechanisms in a low-symmetry crystal field environment [16,33,34].

The corresponding emission spectrum under 377 nm excitation (Fig. 5a, green curve) exhibits intense green luminescence, characteristic of Tb^{3+}, with the dominant $^5D_4 \rightarrow {}^7F_5$ transition centered at 541 nm. Additional emission peaks are also observed at 488 nm ($^5D_4 \rightarrow {}^7F_6$), 583 nm ($^5D_4 \rightarrow {}^7F_4$), 622 nm ($^5D_4 \rightarrow {}^7F_3$), and 672 nm ($^5D_4 \rightarrow {}^7F_1$), reflecting the multiplet nature of the 4f electronic manifold. The energy level diagram in Fig. 5b schematically illustrates the sequential excitation, non-radiative relaxation, and radiative decay pathways responsible for these emissions.

To further understand the excitation-dependent emission behavior, PL spectra were recorded at various excitation wavelengths ranging from 239 to 484 nm for the optimal composition of $x = 3$ wt% Tb^{3+} (Fig. 5c). While the spectral shapes remain consistent, reflecting the stability of the Tb^{3+} coordination environment within the KSGBO host, notable variations in emission intensity were observed. The excitation at 378 nm yielded the strongest emission intensity, indicating that the $^7F_6 \rightarrow {}^5L_9$ transition is particularly efficient in populating the emissive $^5D_4$ state. Similar wavelength-dependent PL efficiency has been reported in other host systems such as $Ca_3La_3(BO_3)_5$ [17] and $Na_2Gd_2B_2O_7$ [20]. The strong excitation-wavelength dependence highlights the importance of matching excitation energy with optimal electronic transitions to maximize luminescence output in real-world optoelectronic applications. The absence of spectral shifts under different excitations further confirms the robustness of the local environment around Tb^{3+} ions in the KSGBO lattice.

To further evaluate the optimal activator concentration, PL emission intensities were measured for KSGBO:$x$$Tb^{3+}$ phosphors ($x = 0.5$–7 wt%) under 378 nm excitation (Fig. 5d). The emission spectra consistently exhibit characteristic Tb^{3+} transitions, dominated by the green $^5D_4 \rightarrow {}^7F_5$

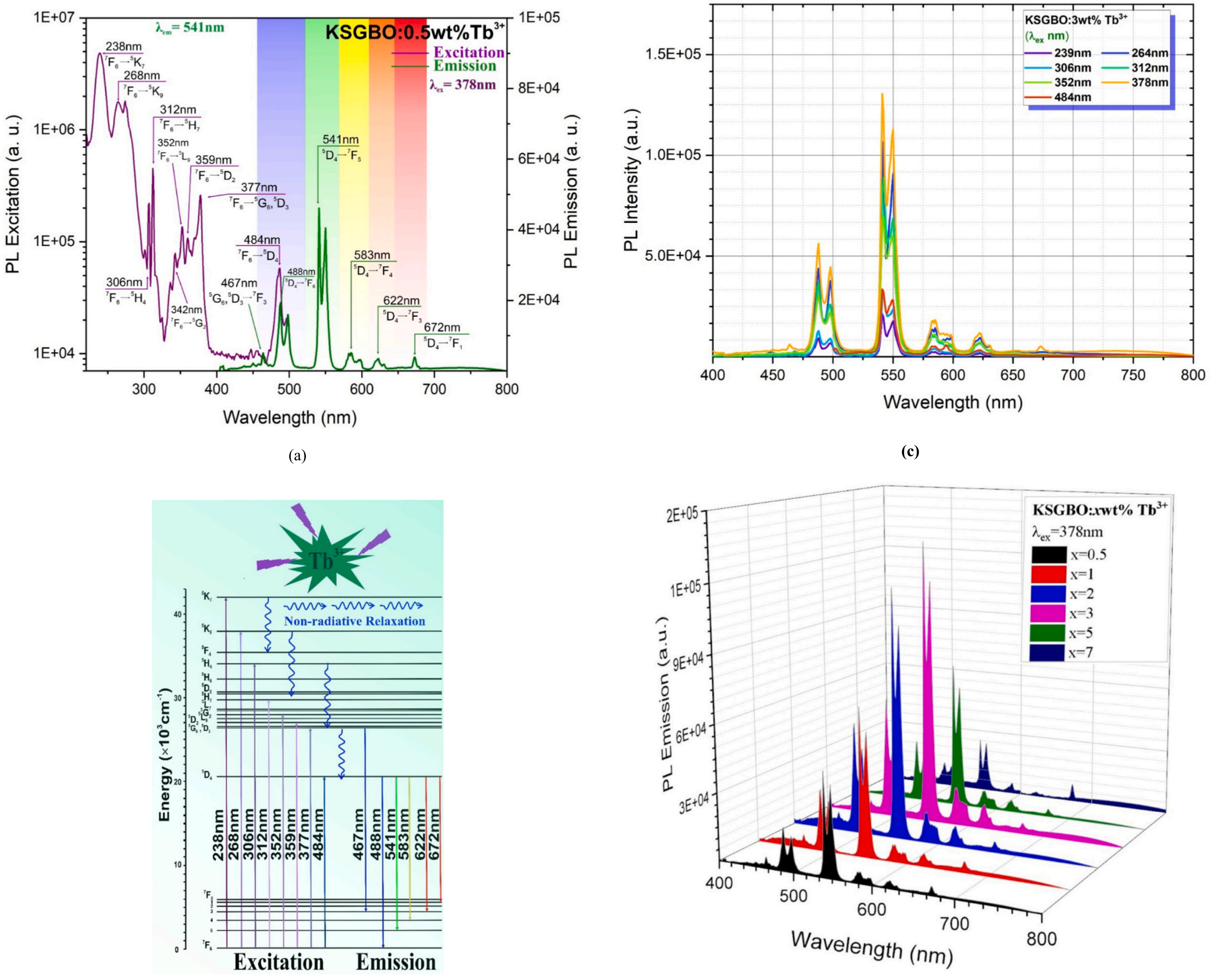

(a)

(c)

(b)

(d)

Fig. 5. (a) Excitation and emission spectra of KSGBO:0.5wt%Tb^{3+} phosphor ($\lambda_{em} = 541$ nm, $\lambda_{ex} = 378$ nm). (b) Energy level diagram of Tb^{3+} showing excitation, non-radiative relaxation, and emission transitions. (c) Emission spectra of KSGBO:3wt%Tb^{3+} under various excitation wavelengths (239–484 nm). (d) Emission spectra of KSGBO:$x$$Tb^{3+}$ ($x = 0.5$–7 wt%) under 378 nm excitation, showing concentration-dependent PL intensity. (e)Linear fit of log (I/x) versus log(x) for KSGBO:$x$$Tb^{3+}$ phosphors in the concentration range $x = 3$–7 wt%.

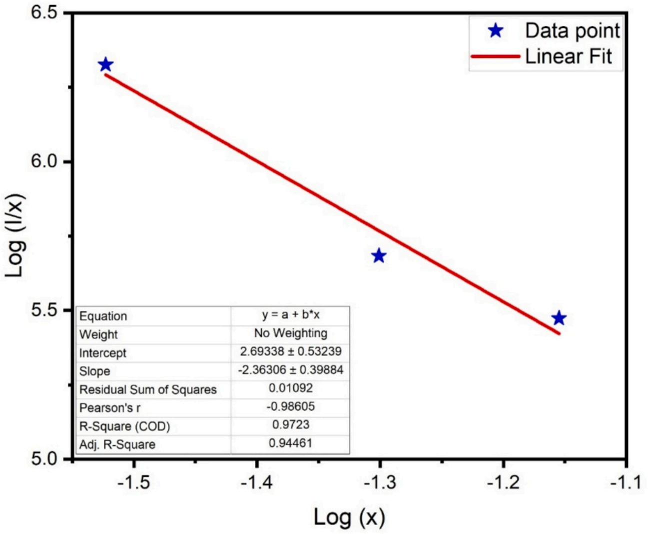

(e)

Fig. 5. (*continued*).

line at 541 nm. As the Tb^{3+} content increases, the emission intensity initially enhances, reaching a maximum at $x = 3$ wt%, and then gradually declines with further doping.

The reduction in luminescence observed beyond the optimal Tb^{3+} concentration is due to concentration quenching, a well-known behavior particularly evident in phosphors containing rare-earth activators. Comparable quenching effects have been attributed to intensified cross-relaxation, while thermally assisted energy migration among neighbouring Tb^{3+} ions has been reported in Tb^{3+}-doped tungstate phosphors [35]. Additionally, at elevated doping levels, energy migration between adjacent Tb^{3+} ions becomes more probable, whereby the excited-state energy of a Tb^{3+} ion ($^5D_4$ level) can be non-radiatively passed to a nearby ion in its ground state. Such energy migration may proceed through mechanisms like exchange coupling or multipolar interactions, which are well-documented in rare-earth systems [36,37]. As the Tb^{3+} concentration increases, the spatial separation between activator ions becomes smaller, enhancing the probability of non-radiative energy transfer through cross-relaxation or multi-phonon processes. Such interactions can facilitate energy migration to quenching centers or defect sites, resulting in a decrease in radiative emission efficiency [35]. Similar luminescence modulation behavior has also been reported in coordination polymer systems, where energy transfer processes and interaction-induced quenching mechanisms significantly influence the emission characteristics [38–41].

The quenching behavior observed here is in agreement with previous studies on borate- and fluoride-based Tb^{3+} phosphors, where the quenching concentration typically falls within the 2–5 mol% range, depending on the host lattice and its energy transfer dynamics [42]. These results confirm that $x = 3$ wt% represents the optimal doping level for maximizing green emission efficiency in the KSGBO host. This optimal doping behavior can be further understood by analyzing the energy migration dynamics illustrated in Fig. 5b. At low Tb^{3+} concentrations, the probability of radiative recombination is high due to well-separated activator ions. However, as the concentration increases beyond the critical level ($x > 3$ wt%), non-radiative processes such as cross-relaxation (CR) become dominant. In particular, the energy level proximity between the $^5D_3 \rightarrow {}^5D_4$ ($\sim$5900 cm^{-1}) and $^7F_6 \rightarrow {}^7F_0$ ($\sim$6000 cm^{-1}) transitions facilitates a CR process between neighbouring Tb^{3+} ions. In this mechanism, the non-radiative relaxation of an excited electron from the $^5D_3$ level in one Tb^{3+} ion is coupled with the simultaneous excitation of another ion from the $^7F_6$ to $^7F_0$ level, followed by eventual decay via multiphonon or defect-mediated pathways. This energy migration and CR lead to depopulation of the emissive $^5D_4$ state, resulting in concentration quenching and reduced PL efficiency at higher doping levels.

To determine the dominant mechanism responsible for concentration quenching in KSGBO:xTb^{3+} phosphors, the critical distance (R_c) for energy transfer between Tb^{3+} ions was estimated. According to Blasse's theory, when R_c exceeds 5 Å, non-radiative energy transfer is most likely governed by multipolar interactions rather than exchange interactions, which dominate at shorter distances [36]. In the present study, the unit cell volume (V) for the sample with the optimal Tb^{3+} concentration ($x =$ 3 wt%) was determined as 2324.782 $Å^3$ from Rietveld refinement. Using the eq. [43]:

$$R_c \approx 2\left[\frac{3V}{4\pi x_c N}\right]^{1/3}$$

where $x_c = 3$ wt% is the critical Tb^{3+} concentration, and $N = 24$ is the number of available cation sites per unit cell, corresponding to the total number of Gd^{3+} sites in the $K_7SrGd_2(B_5O_{10})_3$ structure (2 Gd^{3+} per formula unit with Z = 12 for the trigonal R32 unit cell), since Tb^{3+} ions substitute for Gd^{3+} sites in the host lattice, R_c was calculated to be approximately 14.8 Å. This value significantly exceeds the 5 Å threshold [44], strongly suggesting that the energy transfer responsible for luminescence quenching occurs predominantly via multipole–multipole interactions (MMI) rather than short-range exchange interactions. Although multipolar interaction is identified as the dominant quenching mechanism, contributions from lattice defects, site-to-site disorder, or energy migration via defect-assisted pathways cannot be entirely excluded.

To gain further insight into the concentration quenching mechanism in KSGBO:xTb^{3+} phosphors, the type of multipolar interaction responsible for non-radiative energy transfer was analyzed using Dexter's theoretical framework. According to the model, the nature of multipole–multipole interactions—whether dipole–dipole (d–d), dipole–quadrupole (d–q), or quadrupole–quadrupole (q–q)—can be identified by evaluating the slope of a linear fit to a plot of log(I/x) versus log(x), where I is the PL intensity and x is the Tb^{3+} concentration.

As illustrated in Fig. 5e, the linear fitting of experimental data in the high concentration range (x = 3 wt%–7 wt%) produced a slope of approximately −2.36. Applying Dexter's simplified expression:

$$\log(I/x) = -Q/3\log(x) + K$$

This yields a calculated Q value of ~7.08. Although Q = 7.08 is not an exact match to any ideal multipolar interaction value, it is significantly closer to Q = 6, which corresponds to dipole–dipole (d–d) interaction, than to Q = 8 or 10 (representing d–q or q–q, respectively). Therefore, the dominant energy transfer process leading to concentration quenching in the KSGBO host is most reasonably attributed to dipole–dipole interactions.

This finding aligns with previous reports on similar borate-based hosts doped with Tb^{3+}, where d–d interactions were also found to govern multipolar quenching mechanisms. Such deviation from the theoretical Q value may result from local structural heterogeneities, where non-uniform environments around Tb^{3+} ions affect the dipole–dipole interaction strength or enable competing quenching routes. To further enhance the luminescence performance, alkali ion co-doping strategies were explored and are discussed in the following section.

3.6. *Effect of alkali ion co-doping on PL intensity*

Beyond varying the concentration of the activator ion, another effective strategy for tuning luminescent properties involves co-doping with alkali metal ions. To investigate the effect of alkali ion co-doping on the luminescence properties of KSGBO:3wt%Tb^{3+} phosphors, Li^{+} and Na^{+} ions were introduced into the host lattice in varying concentrations (y = 0–7 wt%), and the resulting emission spectra were recorded under 378 nm excitation (Fig. 6.a–b). A significant enhancement in PL intensity was observed for both co-dopants. Specifically, Li^{+} co-doping resulted in an approximately 4.5-fold increase in the green emission intensity centered at 541 nm, while Na^{+} co-doping yielded an approximately 3-fold enhancement compared to the undoped counterpart.

Similar trends in luminescence enhancement upon alkali ion incorporation have been reported in other rare-earth-activated systems. For instance, Altowyan et al. [19] showed that co-doping Li^{+}, Na^{+}, and K^{+} in Tb^{3+}-activated $YBa_3(BO_3)_3$ phosphors improved crystallinity and modulated local field symmetry, ultimately enhancing radiative transition probabilities and suppressing non-radiative losses. Among them, Li^{+} exhibited the highest enhancement, attributed to its smaller ionic size and more effective lattice distortion. These observations align with previous reports on alkali co-doping in Tb^{3+}-activated hosts. For instance, in (Y, Gd)BO_3:Tb^{3+} phosphors, Li^{+} co-doping significantly enhanced the green emission due to improved energy transfer and crystallinity, as well as induced lattice expansion and morphology refinement, which are attributed to the smaller ionic radius and efficient incorporation of Li^{+} into the host matrix [45].

The luminescence enhancements observed in co-doped KSGBO:Tb^{3+} phosphors can be attributed to several synergistic mechanisms. First, substitution of larger K^{+} ions (1.38 Å) by smaller Li^{+} (0.76 Å) and Na^{+} (1.02 Å) introduces local lattice distortions near Tb^{3+} sites. This local asymmetry perturbs the crystal field and promotes 4f–5d configuration mixing, relaxing parity selection rules and increasing radiative transition rates. Second, alkali ions may passivate residual defect states—such as oxygen vacancies or surface traps—which are known to facilitate non-radiative relaxation. Although direct charge compensation is not required in this system due to the isovalent $Tb^{3+} \leftrightarrow Gd^{3+}$ substitution, alkali ions may still influence defect formation energetics and site symmetry. Third, modified interionic distances and local field fluctuations may optimize energy migration pathways among Tb^{3+} ions, enhancing multipolar interactions while minimizing energy loss through quenching centers.

Between the two alkali co-dopants, Li^{+} induces a more pronounced enhancement than Na^{+}, likely due to its smaller radius and greater polarizing power, resulting in stronger perturbation of the local crystal environment. This observation aligns with previous studies where Li^{+} was found to more effectively improve PL performance in various hosts due to its ability to promote local field asymmetry and crystal refinement. Similar luminescence enhancement mechanisms were also reported in Eu^{3+}-doped Gd_2O_3 phosphors, where co-doping with Li^{+}, Na^{+}, and K^{+} ions improved emission intensity through crystallinity enhancement and local field symmetry modulation, supporting the generality of such effects across lanthanide-activated systems [46].

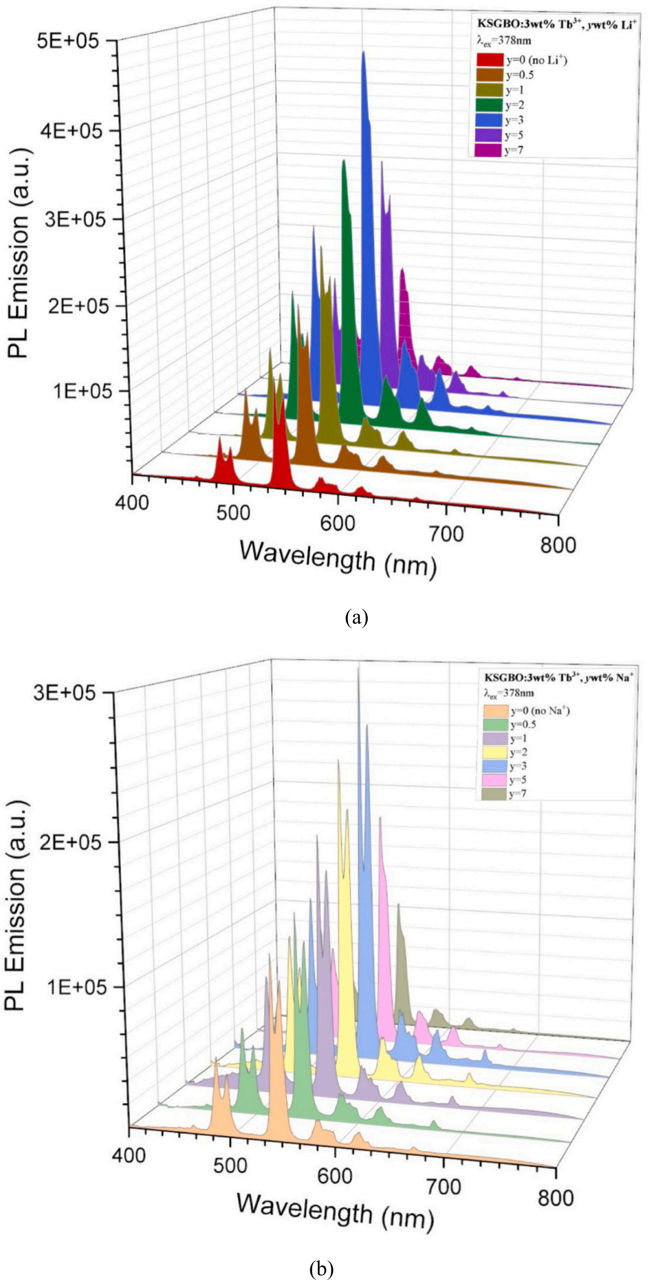

(a)

(b)

Fig. 6. 3D PL emission spectra of (a) KSGBO:3wt%Tb^{3+}, yLi^{+} (b) KSGBO: 3wt% Tb^{3+}, yNa^{+} phosphors under 378 nm excitation as a function of Li^{+} co-doping concentration (y = 0–0.07).

In summary, alkali ion co-doping serves as an effective strategy to enhance the photoluminescence efficiency of Tb^{3+}-activated KSGBO phosphors by concurrently influencing structural, electronic, and vibrational factors that govern radiative recombination.

3.7. *Temperature-dependent PL behavior of KSGBO:3 wt%Tb^{3+} phosphor*

To evaluate the thermal stability and emission behavior of the

KSGBO:3wt%Tb^{3+} phosphor, temperature-dependent PL spectra were recorded in the range of 300–550 K under 378 nm excitation. As shown in the 3D emission map and the corresponding normalized intensity plot (Figs. 7a–b), the green emission band centered at 541 nm exhibits a gradual increase in intensity with temperature. Notably, the PL intensity at 541 nm increases by nearly a factor of two upon heating from 300 K to 550 K, indicating an anomalous temperature-activated luminescence enhancement rather than conventional thermal quenching. Although the temperature-induced enhancement deviates from conventional quenching, an activation energy value could not be extracted due to the non-monotonic nature of the PL response.

Such thermally induced enhancement of Tb^{3+} emission has also been reported in other borate- and tungstate-based hosts. For instance, Kiran et al. [35] observed a similar trend in Ca_2MgWO_6:Tb^{3+} phosphors, where heating enhanced green emission by releasing trapped carriers that subsequently fed the $^5D_4$ excited state of Tb^{3+} ions. This behavior, known as anti-thermal quenching, contrasts the typical decline of PL intensity at elevated temperatures. Similarly, Wang et al. [47] reported an anti-thermal burst behavior in Tb^{3+}-activated $Mg_{1.5}Ca_{0.5}Al_4Si_5O_{18}$ phosphors, where the PL intensity at 544 nm increased significantly up to ~453 K. The authors attributed this anomaly to a combination of negative thermal expansion effects and enhanced internal lattice ordering at elevated temperatures. These observations collectively suggest that thermally driven lattice or symmetry changes may alter the local crystal field around Tb^{3+} ions in a manner that favors radiative over non-radiative decay channels, as previously observed in anti-thermal quenching phosphor systems. A comparable mechanism based on temperature-induced lattice contraction and distortion was demonstrated by Zou et al., where negative thermal expansion strengthened sensitizer-to-activator energy collection at elevated temperatures [48].

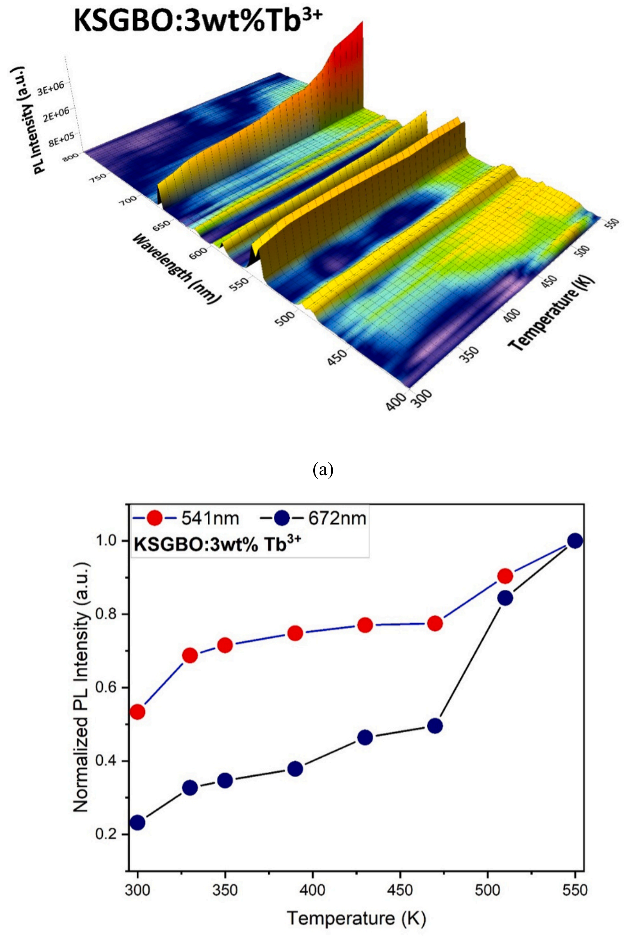

(a)

(b)

Fig. 7. (a) Temperature-dependent 3D PL spectra of KSGBO: 3wt%Tb^{3+} phosphor (300–550 K, λ_{ex} = 378 nm). (b) Normalized intensities of 541 nm ($^5D_4 \rightarrow {}^7F_5$) and 672 nm ($^5D_4 \rightarrow {}^7F_4$) transitions, showing dual-band anti-thermal quenching behavior.

In the present KSGBO:Tb^{3+} system, this enhancement likely arises from multiple temperature-driven processes. First, thermal release of carriers from intrinsic defect-related shallow traps—formed during high-temperature solid-state synthesis—can provide additional excitation pathways for Tb^{3+} ions, effectively compensating for non-radiative losses. Second, moderate lattice expansion at elevated temperatures may slightly reduce multi-phonon relaxation probabilities, thereby favoring radiative recombination from the $^5D_4$ level.

Interestingly, alongside the enhancement of the dominant $^5D_4 \rightarrow {}^7F_5$ green emission at 541 nm, the red emission band at 672 nm ($^5D_4 \rightarrow {}^7F_4$) also shows a pronounced temperature-induced increase (Fig. 7b). While the 541 nm transition is typically dominant in Tb^{3+}-activated phosphors, the concurrent enhancement of the red emission suggests that emission intensity redistributes among the ^7F_J sublevels as temperature rises. This may result from thermal population shifts within the Stark-split ^7F_J manifold or enhanced phonon-assisted relaxation pathways that increase the probability of lower-energy transitions.

Reports of simultaneous thermal enhancement in both green and red Tb^{3+} emission bands are scarce, making this observation particularly noteworthy. The temperature sensitivity of the 672 nm band also points to enhanced influence of crystal field variations or electron–phonon interactions at higher temperatures, subtly modifying the relative transition probabilities. Notably, while such thermally enhanced green emission is frequently reported in Tb^{3+}-activated hosts, the simultaneous and progressive increase in red emission at 672 nm remains a relatively uncommon observation. This dual-band response underscores the presence of complex thermal population dynamics and enhances the multifunctionality of KSGBO:Tb^{3+} for applications requiring multicolor temperature sensitivity. Similar anti-thermal quenching behavior involving thermally assisted enhancement of Tb^{3+} emission has also been observed in Ce^{3+}-sensitized systems, where Ce^{3+} acts as a sensitizer transferring energy to activator ions like Tb^{3+} at elevated temperatures, thereby enhancing PL intensity [49]. In addition, a comparable anti-thermal quenching effect was reported in borate-based hosts such as $Na_2Y_2TeB_2O_{10}$:Tb^{3+} [20,50], attributed to thermally assisted release of carriers from shallow traps, further supporting the role of defect-mediated energy feeding in sustaining emission under heat stress.

Overall, the dual-band anti-thermal quenching behavior observed in KSGBO:3wt%Tb^{3+}—manifested by the simultaneous enhancement of both 541 nm and 672 nm emissions—highlights the presence of thermally activated energy feeding mechanisms and exceptional thermal robustness. This unique temperature response positions the KSGBO:Tb^{3+} phosphor as a promising candidate for high-temperature solid-state lighting and optical thermometry applications, where temperature-induced signal strengthening is advantageous over conventional degradation. The observed anti-thermal quenching behavior cannot be attributed to lifetime extension alone, but rather to thermally assisted carrier release and energy redistribution processes, as further supported by the lifetime analysis discussed later. Notably, this behavior deviates from conventional thermal quenching models such as thermal ionization and crossing relaxation, which typically lead to emission suppression at elevated temperatures [51,52]. Instead, the enhancement observed in KSGBO:Tb^{3+} suggests that thermally driven carrier release and crystal field stabilization play a dominant role in sustaining radiative transitions.

3.8. *Temperature-dependent PL behavior of alkali-co-doped KSGBO:Tb^{3+} phosphors*

To evaluate how alkali ion co-doping influences the thermal luminescence behavior of KSGBO:Tb^{3+} phosphors, temperature-dependent photoluminescence (PL) measurements were conducted on Li^+- and Na^+-modified samples across a temperature range of 300 to 550 K under 378 nm excitation. As illustrated in Figs. 8a–b, both co-doped compositions initially demonstrate an increase in green emission intensity, particularly at 541 nm, indicating a suppression of thermal quenching effects up to around 390 K. This improvement is likely due to thermal activation of trapped carriers or defect-related states, which subsequently facilitate energy transfer to the $^5D_4$ level of Tb^{3+} ions, thereby enhancing the efficiency of radiative recombination.

Interestingly, a similar trend is observed for the red emission band at 672 nm ($^5D_4 \rightarrow {}^7F_4$ transition), which also shows a thermally induced increase up to ~390 K in both samples. This suggests that thermal redistribution of populations among the ^7F_J sublevels, combined with phonon-assisted relaxation, contributes to the enhancement of this typically weak transition. The concurrent rise of both green and red emissions highlights the multilevel nature of the thermal activation processes in these co-doped systems.

However, beyond 390 K, a decline in PL intensity is observed for both Li^+ and Na^+ co-doped samples, signalling the onset of conventional thermal quenching. This drop is likely due to the activation of non-radiative processes such as multi-phonon relaxation or thermal ionization that become dominant at elevated temperatures. Importantly, the thermal quenching onset occurs at nearly the same temperature in both samples, suggesting that while alkali co-doping promotes anti-thermal behavior at moderate temperatures, it does not significantly delay the eventual thermal degradation of PL intensity.

The comparative behavior is further illustrated in Figs. 8c–d, where normalized PL intensities at 541 nm and 672 nm are plotted against temperature. These plots clearly show the initial enhancement followed by quenching, supporting the interpretation that alkali co-doping modifies the trap landscape and energy transfer dynamics, but cannot indefinitely suppress non-radiative losses.

In summary, Li^+ and Na^+ co-doping introduce a beneficial anti-thermal quenching effect in KSGBO:Tb^{3+} phosphors, enhancing both green and red emissions up to ~390 K. This dual-band response reinforces the potential of these materials for temperature-sensitive photonic applications, while also enabling activation energy analysis in the post-quenching regime to gain further insight into thermal deactivation processes.

To gain quantitative insight into the thermal quenching resistance of the alkali co-doped phosphors, the activation energy (E_a) was calculated using the Arrhenius-type eq. [53,54]:

$$\ln\left[\left(\frac{I_0}{I}-1\right)\right]=\frac{E_a}{kT}+C$$

where I_0 and I denote the initial (at 300 K) and temperature-dependent PL intensities, k is the Boltzmann constant, and T is the absolute temperature. The linear fits of $\ln[(I_0/I)-1]$ versus $1/kT$ plots for KSGBO: 3wt%Tb^{3+}, 3wt%Li^+ and KSGBO:3 wt% Tb^{3+},3wt%Na^+ samples are presented in **Fig. 9a** and **b**, respectively.

From the slope values (−0.34958 for Li^+ and − 0.30408 for Na^+), the corresponding E_a values were calculated to be approximately 0.349 eV for the Li^+ co-doped sample and 0.304 eV for the Na^+ co-doped sample. These relatively high activation energies indicate robust resistance to thermally induced non-radiative processes. Notably, the slightly higher E_a for the Li^+-containing sample suggests a marginally enhanced thermal stability, aligning with the comparatively delayed onset of PL

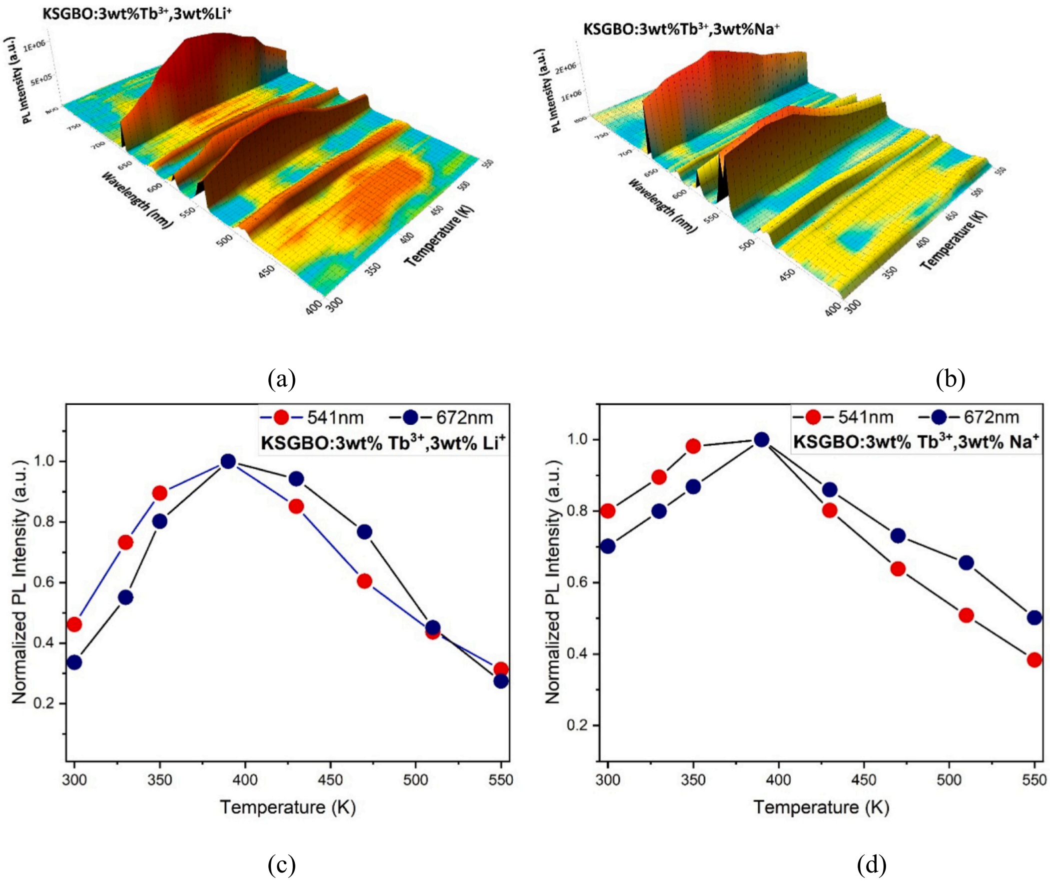

(a) (b)

(c) (d)

Fig. 8. Temperature-dependent PL behavior of KSGBO: 3wt%Tb^{3+} co-doped with Li^+ and Na^+ ions. 3D emission spectra over 300–550 K for (a) Li^+ and (b) Na^+ co-doped samples, respectively. Normalized PL intensities at 541 nm and 672 nm for the (a) Li^+ and (b) co-doped samples.

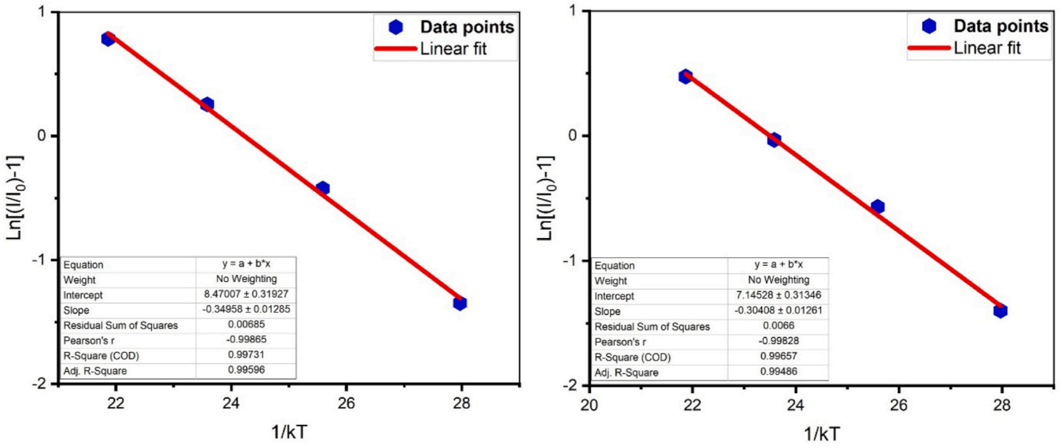

Equation	y = a + b*x
Weight	No Weighting
Intercept	8.47007 ± 0.31927
Slope	-0.34958 ± 0.01285
Residual Sum of Squares	0.00685
Pearson's r	-0.99865
R-Square (COD)	0.99731
Adj. R-Square	0.99596

Equation	y = a + b*x
Weight	No Weighting
Intercept	7.14528 ± 0.31346
Slope	-0.30408 ± 0.01261
Residual Sum of Squares	0.0066
Pearson's r	-0.99828
R-Square (COD)	0.99657
Adj. R-Square	0.99486

(a) (b)

Fig. 9. Arrhenius plots of $\ln[(I_0/I) - 1]$ versus $1/kT$ for (a) KSGBO:3wt%Tb^{3+}, 3wt%Li^{+} and (b) KSGBO:3wt%Tb^{3+}, 3wt%Na^{+} phosphors, used to estimate activation energies for thermal quenching behavior.

intensity decline observed in Fig. 9c.

These findings confirm that alkali co-doping not only introduces dual-band luminescence responsiveness but also improves the thermal endurance of the KSGBO:Tb^{3+} host through effective mitigation of non-radiative relaxation.

3.9. Photoluminescence lifetime analysis

Time-resolved photoluminescence (TRPL) measurements were performed to investigate the decay characteristics and recombination behavior of Tb^{3+}-activated KSGBO phosphors, both in the absence and presence of alkali co-doping. Fig. 10 displays the decay profiles of the 541 nm transition for various compositions, and the corresponding biexponential fitting parameters are summarized in Table 4. The decay curves are well-fitted with a double-exponential model, indicating the presence of multiple recombination pathways:

$$I(t) = A_1 e^{-t/\tau_1} + A_2 e^{-t/\tau_2}$$

Among the single-doped samples, KSGBO:1wt%Tb^{3+} exhibits the longest average lifetime (1.60 ms), which gradually decreases with increasing Tb^{3+} concentration, consistent with increased cross-relaxation and energy migration among adjacent Tb^{3+} ions. Upon alkali co-doping, a moderate decrease in the average lifetime is observed relative to the KSGBO:3wt%Tb^{3+} sample, likely arising from additional non-radiative relaxation channels induced by lattice distortion or charge compensation effects. Notably, the average lifetimes of Li^{+}- and Na^{+}-co-doped samples ($\tau_{avg} \approx 1.15$ ms and 1.20 ms, respectively) remain comparable, indicating that both alkali ions introduce similar levels of non-radiative losses. This observation suggests that neither alkali ion induces a significant alteration in the overall recombination dynamics of the phosphor system.

Table 4

Bi-exponential decay parameters (τ_1, τ_2), relative contributions, average lifetimes (τ_{avg}), and χ^2 values for KSGBO:Tb^{3+} phosphors with varying Tb^{3+} concentrations and alkali metal co-doping.

		Time (ms)	Rel. %	τ_{avg} (ms)	χ^2
KSGBO:1wt%Tb^{3+}	τ_1	0.81	35.74	1.60	1.2618
	τ_2	2.82	64.26		
KSGBO:3 wt%Tb^{3+}	τ_1	0.76	32.91	1.25	1.0959
	τ_2	1.60	67.09		
KSGBO: 5 wt%Tb^{3+}	τ_1	0.68	33.41	1.33	1.2801
	τ_2	1.42	66.59		
KSGBO:3 wt%Tb^{3+}, 3 wt%Li^{+}	τ_1	1.09	36.06	1.15	1.1356
	τ_2	1.20	63.94		
KSGBO:3 wt%Tb^{3+}, 3 wt%Na^{+}	τ_1	0.87	37.44	1.20	1.0656
	τ_2	1.34	62.56		

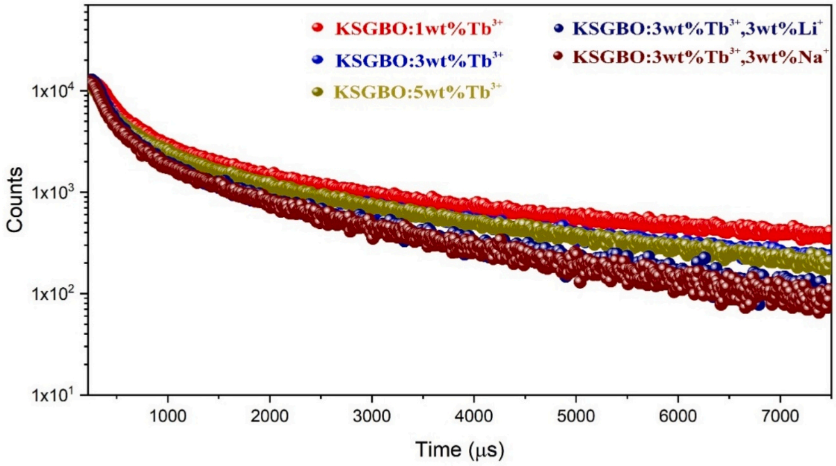

Fig. 10. Time-resolved decay profiles of the $^5D_4 \rightarrow {}^7F_5$ transition at 541 nm for KSGBO:xTb^{3+} (x = 1, 3, 5 wt%) and alkali metal co-doped (Li^{+}, Na^{+}) samples, showing bi-exponential decay behavior and concentration- as well as co-doping-dependent lifetime variations.

These findings confirm that the overall recombination kinetics are only marginally affected by alkali ion type at 3 wt% doping, and that both Li^+ and Na^+ co-doping strategies retain sufficiently long lifetimes for practical photonic applications. Importantly, the co-doping strategy offers clear benefits when compared to traditional phosphors that incorporate only Tb^{3+} as the activator ion. Previously reported Tb^{3+} doped phosphors such as $ZnMoO_4$:Tb^{3+} ($\tau_{avg} \approx 1.03$ ms) [55], $MgAl_2O_4$:Tb^{3+} ($\tau_{avg} \approx 1.0$ ms) [56], and $Na_2Y_2TeB_2O_{10}$:Tb^{3+} ($\tau_{avg} < 1.5$ ms) [50] typically exhibit millisecond-scale lifetimes. In the present KSGBO system, average decay times of ~1.25 ms for Tb^{3+}-only doping and ~ 1.15–1.20 ms upon alkali co-doping fall within this typical range. In comparison, the present KSGBO system combines comparable decay times with improved thermal stability enabled by alkali co-doping.

Although alkali co-doping induces a slight reduction in the average lifetime, this behavior is consistent with the introduction of localized lattice distortions and additional relaxation pathways. Importantly, the preserved millisecond-scale lifetimes, together with the pronounced anti-thermal quenching behavior, suggest that thermally activated energy feeding rather than lifetime prolongation governs the high-temperature luminescence stability of the KSGBO system.

3.10. CIE Chromaticity coordinates and color tuning behavior

To evaluate the chromaticity characteristics of the synthesized

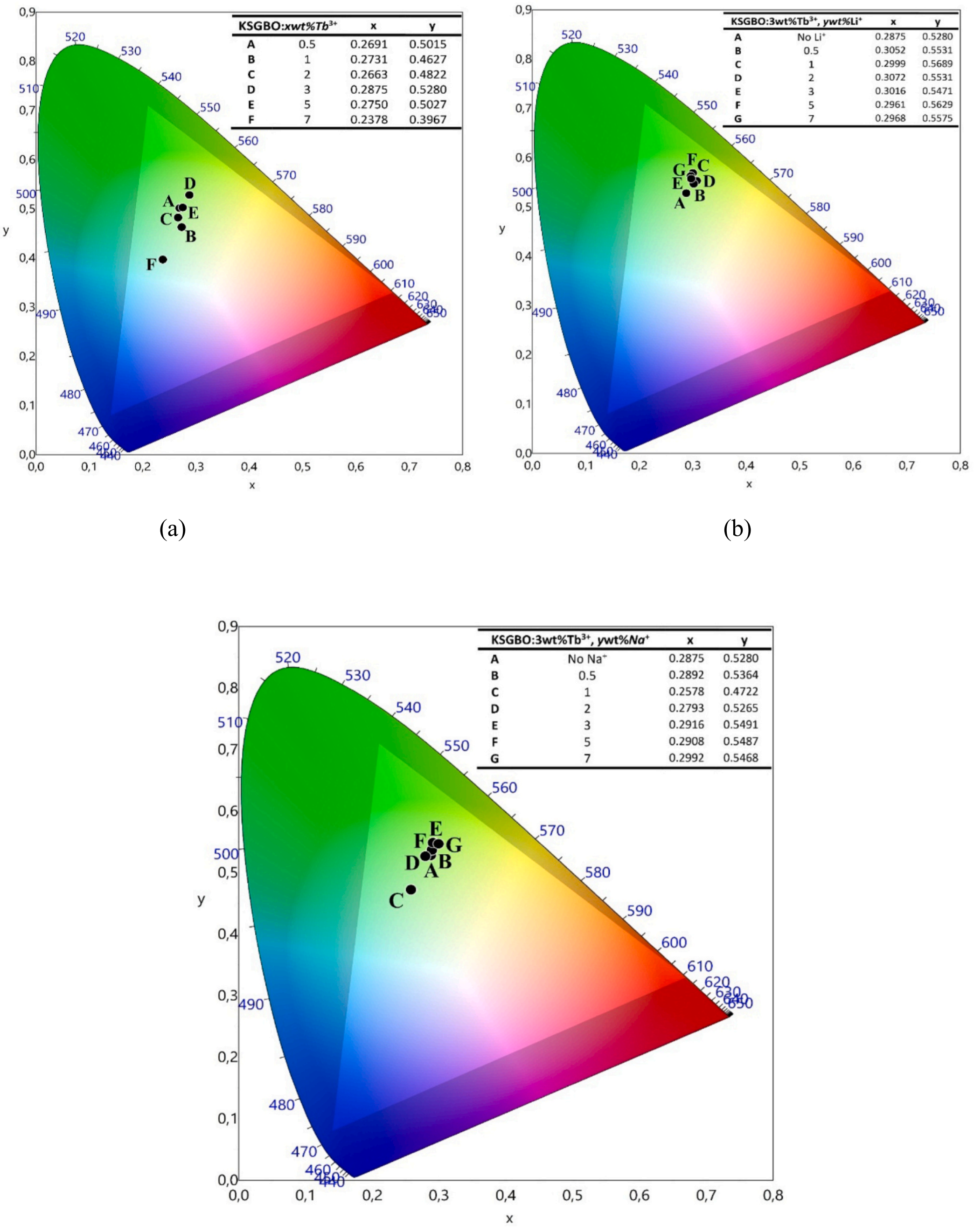

KSGBO:*xwt%Tb*$^{3+}$		x	y
A	0.5	0.2691	0.5015
B	1	0.2731	0.4627
C	2	0.2663	0.4822
D	3	0.2875	0.5280
E	5	0.2750	0.5027
F	7	0.2378	0.3967

(a)

KSGBO:3wt%Tb^{3+}, *ywt%*Li$^+$		x	y
A	No Li$^+$	0.2875	0.5280
B	0.5	0.3052	0.5531
C	1	0.2999	0.5689
D	2	0.3072	0.5531
E	3	0.3016	0.5471
F	5	0.2961	0.5629
G	7	0.2968	0.5575

(b)

KSGBO:3wt%Tb^{3+}, *ywt%Na*$^+$		x	y
A	No Na$^+$	0.2875	0.5280
B	0.5	0.2892	0.5364
C	1	0.2578	0.4722
D	2	0.2793	0.5265
E	3	0.2916	0.5491
F	5	0.2908	0.5487
G	7	0.2992	0.5468

(c)

Fig. 11. CIE 1931 chromaticity diagrams of (a) KSGBO:xTb^{3+} (x = 0.5–7 wt%), (b) KSGBO:3wt%Tb^{3+}, yLi$^+$, and (c) KSGBO:3wt%Tb^{3+}, yNa$^+$ phosphors under 230 nm excitation.

phosphors, CIE 1931 color coordinate diagrams were constructed for various doping conditions (Fig. 11). In the singly doped KSGBO:xTb^{3+} system (Fig. 11a), the emission coordinates shift slightly with increasing Tb^{3+} concentration, reaching a maximum green hue at $x = 3$ wt% before drifting towards the blue region at higher dopant levels (x = 7 wt%), likely due to concentration quenching effects.

This trend is further supported by the calculated correlated color temperature (CCT) and color purity (CP%) values, which show optimal green emission and highest color purity at $x = 3$ wt%, as summarized in Table 5. The correlated color temperature (CCT) values were calculated from the CIE chromaticity coordinates using McCamy's empirical relation [57], where $\mathrm{CCT} = -449n^3 + 3525n^2–6823.3n + 5520.33$ and $n = (x - 0.3320)/(y - 0.1858)$, with ($x$, y) representing the chromaticity coordinates of the sample. Such behavior has also been observed in other green phosphor systems, such as $Mg_{1.5}Ca_{0.5}Al_4Si_5O_{18}$:Tb^{3+}, where increasing Tb^{3+} concentration enhances the $^5D_4 \rightarrow {}^7F_5$ green emission while suppressing blue components, leading to a chromaticity shift towards the upper-right region of the CIE diagram and increased green color purity [58]. In contrast, alkali ion co-doping with Li$^+$ and Na$^+$ produced notably distinct chromatic behaviours (Figs. 11b–c). In the KSGBO:3wt%Tb^{3+}, yLi$^+$ samples, a systematic shift towards higher y values was observed with increasing Li$^+$ content, suggesting improved green color purity. A similar trend was recorded for Na$^+$ co-doped compositions, albeit with slightly different coordinate distributions. This trend is further supported by color purity (CP) values derived from the CIE data (Table 5), where the maximum CP reached 92% for Li$^+$ and 85% for Na$^+$ co-doped samples, compared to a lower 78% in singly doped KSGBO:3wt%Tb^{3+}. These results reflect the capability of alkali co-doping to fine-tune the emission chromaticity, enabling precise color modulation of the phosphor output. Such tunability holds significant potential for designing multicolor or white-emitting phosphor systems for solid-state lighting applications.

The color purity was calculated based on the CIE chromaticity coordinates using the standard relation and reaches up to ~92% for the Li$^+$ co-doped sample, indicating highly saturated green emission. This high color purity originates from the dominant $^5D_4 \rightarrow {}^7F_5$ transition of Tb^{3+} at 541 nm, which produces a narrow-band emission with minimal spectral overlap from other transitions. In addition, the enhancement in color purity upon Li$^+$ co-doping can be attributed to improved local symmetry and reduced lattice defects, which suppress non-radiative relaxation pathways and enhance radiative recombination efficiency.

Table 5
CIE chromaticity coordinates (x, y) and CCT for KSGBO:xTb^{3+}, KSGBO:3wt% Tb^{3+}, yLi$^+$ and KSGBO:3wt%Tb^{3+}, yNa$^+$ phosphors.

Tb^{3+} content (wt%)	***x***	***y***	**CCT**	**CP %**
$x = 0.5$	0.2691	0.5015	7024	70
$x = 1$	0.2731	0.4627	7137	55
$x = 2$	0.2663	0.4822	7212	63
$x = 3$	0.2875	0.5280	6469	78
$x = 5$	0.2750	0.5027	6865	70
$x = 7$	0.2378	0.3967	9316	44
Li$^+$ content (wt%)	***x***	***y***	**CCT**	**CP %**
y = 0.5	0.3052	0.5531	6037	86
y = 1	0.2999	0.5689	6117	92
y = 2	0.3072	0.5531	5998	86
y = 3	0.3016	0.5471	6120	84
y = 5	0.2961	0.5629	6203	90
y = 7	0.2968	0.5575	6199	88
Na$^+$ content (wt%)	***x***	***y***	**CCT**	**CP %**
y = 0.5	0.2892	0.5364	6407	81
y = 1	0.2578	0.4722	7534	61
y = 2	0.2793	0.5265	6662	78
y = 3	0.2916	0.5491	6324	85
y = 5	0.2908	0.5487	6342	85
y = 7	0.2992	0.5468	6170	84

Compared with previously reported Tb^{3+}-activated borate phosphors, the obtained color purity is comparable or superior, confirming the excellent chromatic performance of the KSGBO host. Furthermore, the stable chromaticity coordinates under varying conditions indicate that the emission color is well preserved, which is essential for practical applications in solid-state lighting and display technologies.

In addition to color purity, the correlated color temperature (CCT) values provide further quantitative insight into the chromatic behavior of the phosphors. The calculated CCT values range from ~6000 K to ~9300 K depending on Tb^{3+} and alkali co-doping concentrations, indicating emission characteristics located in the cool green to bluish-green spectral region. Notably, the Li$^+$ co-doped samples exhibit relatively lower CCT values (~6037–6203 K), which are closer to pure green emission and consistent with the shift of the CIE coordinates towards the green region.

The decrease in CCT upon Li$^+$ incorporation correlates with the suppression of blue emission components and the dominance of the narrow-band $^5D_4 \rightarrow {}^7F_5$ transition at 541 nm. In contrast, higher CCT values observed at higher Tb^{3+} concentrations (e.g., $x = 7$ wt%, ~9316 K) indicate an increased contribution of higher-energy (blue) components, consistent with the observed chromaticity shift.

It should also be noted that for Tb^{3+}-based phosphors, the concept of correlated color temperature (CCT) is less meaningful due to the discrete line emission originating from f–f transitions, rather than broadband emission. Therefore, color purity and chromatic stability provide more reliable indicators for evaluating the optical performance of these materials.

4. Conclusion

In summary, Tb^{3+}-activated $K_7SrGd_2(B_5O_{10})_3$ phosphors, modified through Li$^+$/Na$^+$ co-doping, were successfully synthesized as single-phase trigonal pentaborates, with Tb^{3+} ions preferentially occupying Gd^{3+} sites without secondary phase formation. Alkali co-doping induced a slight reduction in unit cell volume, quantified as ~0.22% for Li$^+$ and ~ 0.26% for Na$^+$, indicating lattice relaxation effects due to ionic radius mismatch.

Photoluminescence measurements revealed intense dual-band emission dominated by the green 541 nm transition, with a weaker red emission at 672 nm, and an optimal Tb^{3+} content of 3 wt%, beyond which concentration quenching governed by dipole–dipole interactions occurs. Notably, both the green (541 nm) and red (672 nm) emissions exhibit dual-band anti-thermal quenching, with the 541 nm intensity increasing by nearly a factor of two between 300 and 550 K, demonstrating exceptional thermal stability.

Alkali co-doping further enhanced the green emission intensity by ~4.5-fold (Li$^+$) and ~ 3-fold (Na$^+$) compared to the Tb^{3+}-only sample, while maintaining millisecond-scale decay lifetimes (~1.15–1.20 ms) despite the introduction of minor non-radiative channels. Temperature-dependent analysis yielded activation energies of 0.349 eV (Li$^+$) and 0.304 eV (Na$^+$), confirming strong resistance to thermally activated non-radiative relaxation.

Chromaticity analysis demonstrated tunable (x, y) coordinates and significantly improved green color purity, reaching up to 92% for Li$^+$ co-doped samples.

Overall, the combination of dual-band emission, quantified anti-thermal enhancement, alkali-induced intensity amplification, and high color purity highlights $K_7SrGd_2(B_5O_{10})_3$:Tb^{3+} phosphors—particularly Li$^+$ co-doped compositions—as *promising candidates for next-generation temperature-stable green phosphors* in solid-state lighting, display technologies, and optical thermometry.

Declaration of competing interest

The authors declare that they have no known competing financial interests or personal relationships that could have appeared to influence the work reported in this paper.

Acknowledgements

We would like to express our sincere gratitude to the Research Funds of Balikesir University (Grant No. BAP-2025/013) for the financial support. The authors also acknowledge the Princess Nourah bint Abdulrahman University Researchers Supporting Project (Project No. PNURSP2025R16), Princess Nourah bint Abdulrahman University, Riyadh, Saudi Arabia. We sincerely thank Sezgin Şentürk (Etna Laboratuvar Çözümleri Ltd. Türkiye) and Edinburgh Instruments Ltd. (UK) for their consistent support and intellectual generosity.

Data availability

Data will be made available on request.

References

[1] A. Tiwari, S.J. Dhoble, Borate-based luminescent materials: a comprehensive review of structural influences on thermal stability and luminescence characteristics, J. Lumin. 287 (2025) 121490, https://doi.org/10.1016/j.jlumin.2025.121490.

[2] X. Chen, J. Ni, W. Xiao, X. Song, A new rare-earth borate $Sr_3Dy_2(BO_3)_4$ and tunable luminescence properties of $Sr_3Dy_{2-2x}Eu_{2x}(BO_3)_4$ phosphors, Opt. Mater. 165 (2025) 117119, https://doi.org/10.1016/j.optmat.2025.117119.

[3] O. Madkhali, Ü.H. Kaynar, Y. Alajlani, M.B. Coban, J.G. Guinea, M. Ayvacikli, J. F. Pierson, N. Can, Structural and temperature dependence luminescence characteristics of RE (RE=Eu3+, dy3+, sm3+ and tb3+) in the new gadolinium aluminate borate phosphor, Ceram. Int. 49 (2023) 19982–19995, https://doi.org/10.1016/j.ceramint.2023.03.120.

[4] P.S. Halasyamani, K.R. Poeppelmeier, Noncentrosymmetric oxides, Chem. Mater. 10 (1998) 2753–2769, https://doi.org/10.1021/cm980140w.

[5] Z. Xie, M. Mutailipu, G. He, G. Han, Y. Wang, Z. Yang, M. Zhang, S. Pan, A series of rare-earth borates K7MRE2B15O30 (m = zn, cd, pb; RE = sc, y, gd, lu) with large second harmonic generation responses, Chem. Mater. 30 (2018) 2414–2423, https://doi.org/10.1021/acs.chemmater.8b00491.

[6] W. Liu, X. Liu, J. Shen, Y. Li, H. Song, J. Feng, Z. Lin, G. Zhang, A new non-centrosymmetric gd-based borate crystal Rb7SrGd2(B5O10)3: growth, structure, and nonlinear optical and magnetic properties, Dalt. Trans. 49 (2020) 9355–9361, https://doi.org/10.1039/D0DT01793K.

[7] Y. Wu, J. Liu, P. Fu, J. Wang, H. Zhou, G. Wang, C. Chen, A new lanthanum and calcium borate La2CaB10O19, Chem. Mater. 13 (2001) 753–755, https://doi.org/10.1021/cm0003119.

[8] J. Hakami, Ü.H. Kaynar, M. Ayvacikli, M.B. Coban, J. Garcia-Guinea, P. D. Townsend, M. Oglakci, N. Can, Structural and temperature-dependent luminescence of terbium doped YAl3(BO3)4 phosphor synthesized by the combustion method, Ceram. Int. 48 (2022) 32256–32265, https://doi.org/10.1016/j.ceramint.2022.07.167.

[9] X. Yu, Y. Yue, J. Yao, Z. Hu, $YAl_3(BO_3)_4$: crystal growth and characterization, J. Cryst. Growth 312 (2010) 3029–3033, https://doi.org/10.1016/j.jcrysgro.2010.07.005.

[10] Y. Liu, H. Qi, Q. Lu, F. Yu, Z. Wang, X. Xu, X. Zhao, Type-II second-harmonic-generation properties of YCOB and GdCOB single crystals, Opt. Express 23 (2015) 2163, https://doi.org/10.1364/OE.23.002163.

[11] O. Ayari, C. Bouzidi, F. Khlissa, A. Garbout, S. Hraiech, Investigation of spectroscopic properties of sm3+ doped phosphate glasses for reddish orange light applications, Displays 74 (2022) 102266, https://doi.org/10.1016/j.displa.2022.102266.

[12] J. Dexpert-Ghys, R. Mauricot, B. Caillier, P. Guillot, T. Beaudette, G. Jia, P. A. Tanner, B.-M. Cheng, VUV excitation of YBO3 and (Y,Gd)BO3 phosphors doped with Eu3+ or Tb3+: comparison of efficiencies and effect of site-selectivity, J. Phys. Chem. C 114 (2010) 6681–6689, https://doi.org/10.1021/jp909197t.

[13] R.S. Yadav, A.C. Pandey, Enhanced efficiency in quantum confined YBO3: Tb3+ nanophosphor, J. Alloys Compd. 494 (2010) L15–L19, https://doi.org/10.1016/j.jallcom.2010.01.086.

[14] W. Zhao, S. Gao, S. An, B. Fan, S. Li, The luminescence properties of Sr3Gd(BO3)3: Tb3+ phosphors under vacuum ultraviolet excitation, Chin. Sci. Bull. 57 (2012) 4513–4516, https://doi.org/10.1007/s11434-012-5418-2.

[15] G. Souadi, O. Hakami, U.H. Kaynar, M.B. Coban, H. Aydin, O. Madkhali, T. Zelai, M. Ayvacikli, N. Can, High temperature photoluminescence dependence and energy migration of Tb^{3+}-incorporated $K_3Y(BO_2)_6$ phosphors, Appl. Radiat. Isot. 214 (2024) 111529, https://doi.org/10.1016/j.apradiso.2024.111529.

[16] A.A. Alsam, U.H. Kaynar, H. Aydin, M.B. Coban, A. Canimoglu, N. Can, Enhanced luminescence and quenching mechanisms in na+ co-doped $K_7CaY_2(B_5O_{10})_3$: Tb3+ phosphors under UV radiation, Appl. Radiat. Isot. 217 (2025) 111635, https://doi.org/10.1016/j.apradiso.2024.111635.

[17] M.B. Coban, U.H. Kaynar, A.S. Altowyan, J. Hakami, H. Aydin, A. Canimoglu, N. Can, Judd–Ofelt analysis and negative thermal quenching behavior of Tb^{3+}-activated $Ca_3La_3(BO_3)_5$ phosphors co-doped with alkali ions for high-temperature photonic applications, Sens. Actuators, A Phys. 395 (2025) 117109, https://doi.org/10.1016/j.sna.2025.117109.

[18] H. Orucu, A.S. Altowyan, U.H. Kaynar, H. Aydin, M.B. Coban, J. Hakami, N. Can, Synthesis, structural characterization, and photoluminescence behavior of NaCa4 (BO3)3: Tb3+ phosphors co-doped with k+: insights into radiation-induced defect formation and charge compensation via DFT calculations, Appl. Radiat. Isot. 225 (2025) 112038, https://doi.org/10.1016/j.apradiso.2025.112038.

[19] A.S. Altowyan, U.H. Kaynar, C. Gök, H. Aydin, J. Hakami, M.B. Coban, A. Canimoglu, N. Can, Photoluminescence characteristics and Judd–Ofelt analysis of $YBa_3(BO_3)_3$:Tb^{3+} phosphors co-doped with Li^+, Na^+, and K^+, J. Lumin. 286 (2025) 121380 https://doi.org/10.1016/j.jlumin.2025.121380.

[20] G. Souadi, M.B. Coban, U.H. Kaynar, H. Aydin, S.C. Kaynar, V. Onar, A. Canimoglu, H.J. Alathlawi, N. Can, Structural and luminescence properties of Tb^{3+}-doped $Na_2Gd_2B_2O_7$ phosphors for LED applications: Judd–Ofelt analysis and alkali co-doping effects, J. Ind. Eng. Chem. 153 (2026) 742–758, https://doi.org/10.1016/j.jiec.2025.07.037.

[21] Z. Ren, C. Tao, H. Yang, Synthesis and luminescent characterization of YAl3(BO3) 4: Tb3+ phosphors, J. Mater. Sci. Mater. Electron. 19 (2008) 319–321, https://doi.org/10.1007/s10854-007-9320-7.

[22] L. Zhang, W. Xu, X. Yang, L. Yu, H. Yang, Luminescent properties of GdAl3(BO3)4: Ln3+ (ln3+: Eu3+, tb3+, dy3+) nano-phosphors, J. Mater. Sci. Mater. Electron. 23 (2012) 1031–1036, https://doi.org/10.1007/s10854-011-0542-3.

[23] V.R. Panse, S.P. Hargunani, A. Saregar, S.M. Waghare, A. Hadap, S.V. Dewalkar, Y. Yuberti, Analyzing the photoluminescence and energy transfer in Sr3Gd(BO3)3: inorganic borate-based phosphor eu3+, tb3+ and ce3+, J. Opt. 55 (2026) 431–440, https://doi.org/10.1007/s12596-024-02077-5.

[24] G. Souadi, A.Y. Madkhli, U.H. Kaynar, C. Gok, H. Aydin, M.B. Coban, S.C. Kaynar, M. Ayvacikli, N. Can, Photoluminescence properties and structural analysis of tb3+−doped $K_3Gd(BO_2)_6$: a first study on negative thermal quenching, J. Alloys Compd. 1010 (2025) 178147, https://doi.org/10.1016/j.jallcom.2024.178147.

[25] C. Guo, H. Jing, T. Li, Green-emitting phosphor Na2Gd2B2O7: Ce3+, tb3+ for near-UV LEDs, RSC Adv. 2 (2012) 2119, https://doi.org/10.1039/c2ra00808d.

[26] A. Monshi, M.R. Foroughi, M.R. Monshi, Modified scherrer equation to estimate more accurately Nano-crystallite size using XRD, World J. Nano Sci. Eng. 02 (2012) 154–160, https://doi.org/10.4236/wjnse.2012.23020.

[27] G. Williamson, W. Hall, X-ray line broadening from filed aluminium and wolfram, Acta Metall. 1 (1953) 22–31, https://doi.org/10.1016/0001-6160(53)90006-6.

[28] N.C. Halder, C.N.J. Wagner, Separation of particle size and lattice strain in integral breadth measurements, Acta Crystallogr. 20 (1966) 312–313, https://doi.org/10.1107/S0365110X66000628.

[29] B.D. Cullity, S.R. Stock, Elements of X-Ray Diffraction, third ed., Prentice Hall, 2014.

[30] S.Y. Marzouk, M.A. Azooz, H.M. Elsaghier, N.A. Zidan, W. Abbas, Structural and optical properties of barium titanium borate glasses doped with ytterbium, J. Mater. Sci. Mater. Electron. 33 (2022) 18054–18071, https://doi.org/10.1007/s10854-022-08665-0.

[31] P. Kumar, S. Meena, Menka meena, nitiksha sharma, beena bhatia, structural characterization, raman spectroscopy and FTIR spectroscopy studies of pr3+ doped tellurium bismuth borate glasses, J. Condens. Matter 3 (2025) 103–105, https://doi.org/10.61343/jcm.v3i01.93.

[32] C.S. Pavan Kumar, S. Pratap, C.S. Sumuka, N. Sivasankara Reddy, Review on the structure of borate glasses by raman spectroscopic technique, Ceram. Int. (2025), https://doi.org/10.1016/j.ceramint.2025.12.004.

[33] U. Fawad, H.J. Kim, I. Gul, M. Khan, S. Tahir, T. Jamal, W. Muhammad, Proton, UV, and x-ray induced luminescence in tb3+ doped LuGd2Ga2Al3O12 phosphors, Crystals 10 (2020) 844, https://doi.org/10.3390/cryst10090844.

[34] F. Xia, S. Liu, Y. Wang, J. Mao, X. Li, Y. Wang, G. Chen, Fast and intense green emission of tb3+ in borosilicate glass modified by cu+, Sci. Rep. 5 (2015) 15387 https://doi.org/10.1038/srep15387.

[35] R. Kiran, S.M.M. Kennedy, A. Princy, M.I. Sayyed, A.H. Almuqrin, S.D. Kamath, Negative thermal quenching and optically stable tb3+ −doped tungstate phosphor for high temperature lighting and advanced thermometry applications, Mater. Adv. 6 (2025) 9746–9760, https://doi.org/10.1039/D5MA00655D.

[36] G. Blasse, A. Bril, Photoluminescent efficiency of phosphors with electronic transitions in localized centers, J. Electrochem. Soc. 115 (1968) 1067, https://doi.org/10.1149/1.2410880.

[37] G. Blasse, M.G.J. van Leur, Luminescence and energy transfer in the columbite structure, Mater. Res. Bull. 20 (1985) 1037–1045, https://doi.org/10.1016/0025-5408(85)90202-8.

[38] M. Kukreja, M. Ahmad, N. Haq, A.A. Kumar, K.A. Siddiqui, Enhanced luminescence sensing of pymetrozine pesticide in cow milk using a cd(II) coordination network with sensitivity up to 0.448 ppm, New J. Chem. 49 (2025) 2703–2721, https://doi.org/10.1039/D4NJ04487H.

[39] P. Sharma, N. Haq, M. Ahmad, K.A. Siddiqui, Mo@zinc-CP composite for dual applications: luminescent detection of pesticides and photodegradation of organic dyes, J. Mol. Struct. 1327 (2025) 141249, https://doi.org/10.1016/j.molstruc.2024.141249.

[40] A. Afzal, M. Ahmad, N. Haq, A.A. Kumar, D. Dewangan, R. Medishetty, K. A. Siddiqui, A multifunctional [H2BTC]2−·[Zn(H2O)6]2+ hydrogen-bonded coordination network: An efficient detection of 2,4-D amine herbicide and photodegradation of RB dye, Polyhedron 281 (2025) 117718, https://doi.org/10.1016/j.poly.2025.117718.

[41] A. Ahmed, M. Ahmad, C. Thakur, A.A. Kumar, N. Lee, N. Haq, K.A. Siddiqui, NiS2 -integrated cd-oxalate MOF: a multifunctional platform for selective 2,4- d amine sensing and efficient NR/EBT photodegradation, CrystEngComm (2026), https://doi.org/10.1039/D5CE01183C.

[42] L. Huang, X. Wang, H. Lin, X. Liu, Luminescence properties of ce3+ and tb3+ doped rare earth borate glasses, J. Alloys Compd. 316 (2001) 256–259, https://doi.org/10.1016/S0925-8388(00)01432-8.

[43] C.M. Nandanwar, N.S. Kokode, R.M. Yerojwar, A.N. Yerpude, Combustion synthesis and photoluminescence study of novel sm3+ activated K3La(PO4)2 phosphor for n-UV solid state lighting, Nano-Structures & Nano-Objects 36 (2023) 101068, https://doi.org/10.1016/j.nanoso.2023.101068.

[44] D.L. Dexter, A theory of sensitized luminescence in solids, J. Chem. Phys. 21 (1953) 836–850, https://doi.org/10.1063/1.1699044.

[45] H. Xu, W. Zhuang, X. Wen, R. Liu, Y. Hu, T. Xia, Effect of Li$^+$ ions doping on structure and luminescence of (Y,Gd)BO$_3$:Tb^{3+}, J. Rare Earths 28 (2010) 701–704, https://doi.org/10.1016/S1002-0721(09)60183-6.

[46] N. Dhananjaya, H. Nagabhushana, B.M. Nagabhushana, B. Rudraswamy, C. Shivakumara, K. Narahari, R.P.S. Chakradhar, Enhanced photoluminescence of Gd2O3: Eu3+ nanophosphors with alkali (M=Li+, na+, k+) metal ion co-doping, Spectrochim. Acta A Mol. Biomol. Spectrosc. 86 (2012) 8–14, https://doi.org/10.1016/j.saa.2011.05.072.

[47] L. Wang, Z. Bai, H. Sun, H. Tang, X. Liu, L. Chen, Structure and luminescence properties of tb3+−doped Mg1.5Ca0.5Al4Si5O18 green phosphors with anti-thermal burst effect, J. Alloys Compd. 1039 (2025) 183140, https://doi.org/10.1016/j.jallcom.2025.183140.

[48] H. Zou, X. Yang, B. Chen, Y. Du, B. Ren, X. Sun, X. Qiao, Q. Zhang, F. Wang, Thermal enhancement of upconversion by negative lattice expansion in orthorhombic Yb2W3O12, Angew. Chemie Int. Ed. 58 (2019) 17255–17259, https://doi.org/10.1002/anie.201910277.

[49] Y. Li, Y. Zhou, X. Li, H. Wu, L. Zhao, W. Wang, Energy transfer and the anti-thermal quenching behavior of Sr8MgCe(PO4)7: Tb3+ for temperature sensing, spectrochim, Acta Part A Mol. Biomol. Spectrosc. 252 (2021) 119548, https://doi.org/10.1016/j.saa.2021.119548.

[50] Y. Xiang, L. Yang, C. Liao, X. Xiang, X. Tang, H. Tang, J. Zhu, Thermometric properties of Na2Y2TeB2O10: Tb3+ green phosphor based on fluorescence/excitation intensity ratio, J. Adv. Ceram. 12 (2023) 848–860, https://doi.org/10.26599/JAC.2023.9220725.

[51] Y. Liu, J. Silver, R.-J. Xie, J. Zhang, H. Xu, H. Shao, J. Jiang, H. Jiang, An excellent cyan-emitting orthosilicate phosphor for NUV-pumped white LED application, J. Mater. Chem. C 5 (2017) 12365–12377, https://doi.org/10.1039/C7TC04168C.

[52] J. Zhong, W. Zhuang, X. Xing, R. Liu, Y. Li, Y. Liu, Y. Hu, Synthesis, crystal structures, and photoluminescence properties of Ce3+-doped Ca2LaZr2Ga3O12: new garnet green-emitting phosphors for white LEDs, J. Phys. Chem. C 119 (2015) 5562–5569, https://doi.org/10.1021/jp508409r.

[53] V. Rajagopal, X. Huang, Y. Wu, Tunable luminescence and energy transfer in novel blue-green-emitting BaGd2Si3O10:Ce3+,Tb3+ phosphors for near-UV-based white LEDs, ACS Omega 4 (2019) 4384–4389, https://doi.org/10.1021/acsomega.9b00182.

[54] H. Guo, X. Huang, Y. Zeng, Synthesis and photoluminescence properties of novel highly thermal-stable red-emitting Na3Sc2(PO4)3: Eu3+ phosphors for UV-excited white-light-emitting diodes, J. Alloys Compd. 741 (2018) 300–306, https://doi.org/10.1016/j.jallcom.2017.12.316.

[55] L.X. Lovisa, Y.L.R.L. Fernandes, L.M.P. Garcia, B.S. Barros, E. Longo, C. A. Paskocimas, M.R.D. Bomio, F.V. Motta, Tb^{3+}/Pr^{3+} co-doped ZnMoO$_4$ phosphor with tunable photoluminescence and energy transfer processes, Opt. Mater. 96 (2019) 109332, https://doi.org/10.1016/j.optmat.2019.109332.

[56] S. Zhongxiang, S. Jun, W. Jing, L. Yang, L. Yongfu, Preparation and spectral properties of MgAl2O4: Tb3+ phosphor, Spectroscopy (2023) 28–34, https://doi.org/10.56530/spectroscopy.xr3287v2.

[57] C.S. McCamy, Correlated color temperature as an explicit function of chromaticity coordinates, Color Res. Appl. 17 (1992) 142–144, https://doi.org/10.1002/col.5080170211.

[58] J. Chen, L. Hu, J. Deng, X. Xing, Negative thermal expansion in functional materials: controllable thermal expansion by chemical modifications, Chem. Soc. Rev. 44 (2015) 3522–3567, https://doi.org/10.1039/C4CS00461B.